frontiers in Earth Science

ORIGINAL RESEARCH
published: 27 August 2021
doi: 10.3389/feart.2021.642667

Morpho-Mineralogical and Bio-Geochemical Description of Cave Manganese Stromatolite-Like Patinas (Grotta del Cervo, Central Italy) and Hints on Their Paleohydrological-Driven Genesis

Simone Bernardini[1], Fabio Bellatreccia[1,2], Andrea Columbu[3], Ilaria Vaccarelli[4], Marika Pellegrini[4], Valme Jurado[5], Maddalena Del Gallo[4], Cesareo Saiz-Jimenez[5], Armida Sodo[1], Christian Millo[6], Luigi Jovane[6] and Jo De Waele[3]*

[1]Dipartimento di Scienze, Università Roma Tre, Roma, Italy, [2]Istituto Nazionale di Fisica Nucleare – Laboratori Nazionali di Frascati (INFN-LNF), Frascati (Roma), Italy, [3]Dipartimento di Scienze Biologiche, Geologiche e Ambientali, Università di Bologna, Bologna, Italy, [4]Dip. MeSVA, Sezione di Scienze Ambientali, Università dell'Aquila, L'Aquila, Italy, [5]Instituto de Recursos Naturales y Agrobiologia (IRNAS-CSIC), Sevilla, Spain, [6]Instituto Oceanográfico, Universidade de São Paulo, São Paulo, Brazil

OPEN ACCESS

Edited by:
Aurel Persoiu, Emil Racovita Institute of Speleology, Romania

Reviewed by:
Laura Rosales-Lagarde, Nevada State College, United States
Cristina Purcarea, Institute of Biology Bucharest of the Romanian Academy, Romania

***Correspondence:**
Simone Bernardini
simone.bernardini@uniroma3.it

Specialty section:
This article was submitted to Sedimentology, Stratigraphy and Diagenesis, a section of the journal Frontiers in Earth Science

Received: *16 December 2020*
Accepted: *30 July 2021*
Published: *27 August 2021*

Citation:
Bernardini S, Bellatreccia F, Columbu A, Vaccarelli I, Pellegrini M, Jurado V, Del Gallo M, Saiz-Jimenez C, Sodo A, Millo C, Jovane L and De Waele J (2021) Morpho-Mineralogical and Bio-Geochemical Description of Cave Manganese Stromatolite-Like Patinas (Grotta del Cervo, Central Italy) and Hints on Their Paleohydrological-Driven Genesis. Front. Earth Sci. 9:642667. doi: 10.3389/feart.2021.642667

Caves are dark subsurface environments with relatively constant temperatures that allow studying bio-mineralization processes and paleoenvironmental or climate changes in optimal conditions. In the extreme and oligotrophic cave environment, manganese patinas having stromatolite-like features are uncommon. Here we provide the first detailed mineralogical, geochemical, and microbiological investigation of fine-grained and poorly crystalline MnFe stromatolite-like wall patinas formed in a deep-cave environment in Italy. These mineralizations, about 3 mm thick, consist of an alternation of Mn-layers and Fe-lenses. We show that the microbial communities' composition is dominated by Mn-oxidizing bacteria, such as *Bacillus*, *Flavobacterium*, and *Pseudomonas*. Our multidisciplinary investigation, integrating data from different analytical techniques (*i.e.,* optical microscopy, SEM-EDS, μXRF, XRPD, FT-IR, Raman spectroscopy, and DNA sequencing), revealed peculiar chemical, mineralogical, and biological features: 1) A cyclical oscillation of Mn and Fe along the growth of the patinas. We propose that this oscillation represents the shift between oxic and suboxic conditions related to different phases occurring during paleo-flood events; 2) A typical spatial distribution of mineralogy and oxidation state of Mn, bacterial imprints, detrital content, and stromatolite-like morphologies along the Mn-layers. We propose that this distribution is controlled by the local hydraulic regime of the paleo-floods, which, in turn, is directly related to the morphology of the wall surface. Under less turbulent conditions, the combination of clay mineral catalysis and biological oxidation produced vernadite, a poor-crystalline phyllomanganate with a low average oxidation state of Mn, and branched columnar stromatolite-like morphologies. On the other hand, under more turbulent conditions, the sedimentation of clay minerals and microbial communities' development are both inhibited. In this local environment, a lower oxidation rate of

Mn^{2+} favored the formation of todorokite and/or ranciéite, two compounds with a high average oxidation state of Mn, and flat-laminated or columnar stromatolite-like morphologies.

Keywords: cave deposits, karst system, MnFe patinas, bio-mineralization, biogeochemical processes, paleoenvironmental changes

INTRODUCTION

Manganese oxides/hydroxides/oxyhydroxides (hereafter MnOx) are important geomaterials, widespread in terrestrial and Martian geological records, and related to hydrothermal activity, authigenesis or sedimentary/weathering processes (Roy et al., 1997; Lanza et al., 2014, 2016; Arvidson et al., 2016). In natural environments, the mineralogy and oxidation state of Mn are strongly controlled by ambient conditions (*e.g.,* pH, Eh, ionic strength, and microbial activity). MnOx crystal structures result from the linkage of MnO_6 octahedra forming channel or layered structures, in which Mn occurs under different oxidation states (*e.g.*, Mn^{2+}, Mn^{3+}, and Mn^{4+}) (Post, 1999). MnOx occur typically as poorly crystalline material and mixtures of different Mn-compounds with Fe oxides/hydroxides, silicates, and carbonates; thus, their characterization by standard methods, such as X-ray powder diffraction (XRPD), is extremely challenging and not always conclusive. For instance, X-ray patterns are characterized by broad and weak reflections of MnOx, which can be easily overlapped by the stronger reflections of the intermixed silicates and carbonates. Spectroscopic techniques, such as Fourier-Transform Infrared (FT-IR) and Raman spectroscopy, sensitive to short-range metal-oxygen arrangements, provide a valuable tool for characterizing MnOx. Raman spectroscopy, in particular, is a very powerful technique to characterize MnOx, being suitable for disordered and/or poorly crystalline materials (Bernardini et al., 2019). In some cases, all these techniques need to be used to characterize such disordered and cryptocrystalline mixtures properly. Moreover, Raman spectroscopy is useful also for the microanalysis of the oxidation state of Mn in MnOx at sub-micrometric spatial resolution (Bernardini et al., 2020a).

MnFe mineral deposits in caves are well known (Hill and Forti, 1997, and references therein). Gázquez et al. (2011) described two types of MnFe occurrences in caves: 1) MnFe minerals deposited by running water, with no weathering of the underlying substratum, and 2) deposits linked to weathering of the host rock. The latter, relatively scarce in caves, was found in Sima de la Higuera Cave (Spain) and other hypogenic caves such as Spider Cave, Lechuguilla Cave, Jewel Cave, and Wind Cave (United States). Generally, these deposits consist of MnOx associated with Fe oxides/hydroxides and detrital or authigenic minerals, such as quartz and clay minerals. They occur as black crusts or patinas coating the walls of the caves and the stream clasts, as stains on speleothems, or as black sedimentary fill deposits (Hill and Forti, 1997). Accordingly, a multimethodological approach is necessary to characterize such disordered and cryptocrystalline mixtures properly. In the last decades, several authors have investigated the mineralogy of MnOx in caves by using different analytical techniques. Northup et al. (2000) identified todorokite from the Lechuguilla and Spider Caves (New Mexico, USA) by SEM-EDS and TEM. The same result was obtained by Cunningham et al. (1995) using SEM-EDS and XRPD. Spilde et al. (2005), integrating SEM-EDS, XRF, XRPD, and TEM results, identified todorokite and lithiophorite. Carmichael et al. (2013a), combining SEM-EDS, single-crystal micro-XRD, and FT-IR data, identified buserite and todorokite in the Carter Saltpeter Cave system, Tennessee (USA). Frierdich et al. (2011) identified birnessite and buserite from the Pautler Cave, Illinois (USA) by SEM-EDS and XRPD. White et al. (2009) studied the mineralogy of Mn-coatings in 15 caves in the United States by combining SEM-EDS, XRPD, and FT-IR data. Still, the low crystallinity of MnOx, together with other impurities, prevented proper phase(s) identification by XRPD. These authors have only attempted to assign the FT-IR spectra to different phases, such as birnessite, romanèchite, ranciéite, and pyrolusite. Papier et al. (2011), even though combining SEM-EDS, XRPD, FT-IR, and Raman spectroscopy data could not obtain a conclusive phase determination of samples from the Azé Cave, Saône-et-Loire (France). Gázquez et al. (2011) identified birnessite and goethite by XRD in black MnFe crusts from speleothems of El Soplao Cave (Spain). Rossi et al. (2010), investigating the same mineralizations by XRD and FT-IR, identified hausmannite, birnessite, ranciéite, and goethite.

In many natural environments, bacteria and fungi catalyze the oxidation of Mn^{2+} and the formation of poorly crystalline $Mn^{3+/4+}$ oxides, with an average oxidation state of Mn commonly higher than 3.4 (Tebo et al., 2004). Andrejchuk and Klimchouk (2001) and Kotula et al. (2019) described MnFe sediments from Zoloushka Cave (Ukraine/Moldova), whose formation may have been mediated by heterotrophic and autotrophic bacteria (Kotula et al., 2019). Fonollá et al. (2020) described MnFe crusts from Majada del Cura Cave (Spain). They consist of Fe oxides/hydroxides (the predominant mineral is goethite), MnOx, and silicate minerals. These authors related the formation of these crusts to the subterranean river's hydrogeomorphological evolution and bacterial activity. Rossi et al. (2010) described MnOx stromatolites in El Soplao Cave (Spain). These mineralizations show well preserved fossils of Mn-oxidizing bacteria, including genera as *Hyphomicrobium*, *Pedomicrobium*, and *Caulobacter*, which underwent low diagenetic alteration thanks to the relatively high accretion rates of the MnOx stromatolites (Lozano and Rossi, 2012). Gradziński et al. (1995) described biogenic Mn flowstones from Jaskinia Czarna Cave (Poland). These mineralizations consist of amorphous MnOx and are characterized by a dome-like structure and a high Mn/Fe ratio

(~72). Northup et al. (2003) investigated MnFe deposits in Lechuguilla and Spider caves to assess which biotic factors may be involved in their formation and study the microbial community's nature thriving in the deposits. These authors identified the presence of bacteria whose closest relatives are Fe- and Mn-oxidizing/reducing bacteria, including *Hyphomicrobium, Pedomicrobium, Leptospirillum, Stenotrophomonas*, *Pantoea* genera, in addition to representative of the *Crenarchaeota* and *Euryarchaeota* archaeal phyla. However, the extent to which Fe- and Mn-oxidizing bacteria contribute to the production of MnFe deposits in these caves is still not fully understood.

In the last decades, the role of a few bacteria in the production of MnOx was investigated in detail (Villalobos et al., 2003; Tebo et al., 2005; Spiro et al., 2010). Carmichael et al. (2015) reviewed the role of Mn-oxidizing microorganisms in caves and concluded that bacteria and fungi produced MnOx minerals, which are typically dark brown to black, and poorly crystalline, with birnessite or todorokite crystal structures. These authors reported several bacterial strains, included in the genera *Flavobacterium, Bacillus, Pseudomonas, Hyphomicrobium, Pedomicrobium, Leptothrix,* and *Pantoea*, among others. In addition, based on TEM, FE-SEM, X-ray microanalysis, and FT-IR, Saiz-Jimenez et al. (2012) proved the biogenic deposition of birnessite by the fungus *Acremonium nepalense* on the clayey sediments of Lascaux Cave.

A fundamental geochemical property of Mn is its high redox sensitivity. Compared to Fe compounds, MnOx are stable only under basic pH conditions (>8), except at high Eh (>600 mV) (Hem, 1963, 1972). Therefore, the presence/absence of Fe and Mn minerals allows recognizing different redox environments (Berner, 1981). Because of the different redox-sensitive behaviour of Mn and Fe, the Mn/Fe ratio can be successfully used to reconstruct changing redox conditions, being lower ratios related to lower O_2 concentrations in the water system (Naeher et al., 2013 and references therein). Accordingly, MnFe mineralizations can be successfully used as paleo-redox indicators to reconstruct environmental and climate changes in the geological past, in cave (see Gázquez et al., 2011), oceanic (Hein et al., 2017; Benites et al., 2018; Robertson et al., 2019; Cornaggia et al., 2020), and lake environments (Naeher et al., 2013). Moreover, because of their high specific surface area (~300 m^2/g) and low point of zero charge (PZC < 3) MnOx strongly control the mobility and availability of rare earth elements and heavy metals in aqueous systems (McKenzie, 1980; Oscarson et al., 1983; Koschinsky and Halbach, 1995). Cave secondary deposits offer the opportunity to investigate past hydrological changes, at times demonstrating climate forcing (Fairchild et al., 2006). Accordingly, numerous studies have been carried from northern (Frisia et al., 2005; Zanchetta et al., 2007; Drysdale et al., 2009; Belli et al., 2013; Columbu et al., 2018; Regattieri et al., 2019) to central (Vanghi et al., 2018), southern (Columbu et al., 2020) and insular (Frisia et al., 2006; Columbu et al., 2017, 2019) Italy. Indeed, with constant temperature and absence of light, cave environments offer ideal conditions to study various topics, like paleo-environmental and climate change, the origin and evolution of life, and bio-mineralization processes, among others. However, the study of the hydrological, environmental and climate significance of speleothems other than stalagmites and flowstones in Italy is still underrepresented compared to other countries (Hill and Forti, 1997).

This work aims to provide the first mineralogical, geochemical, and microbiological investigation of fine-grained and poorly crystalline MnFe cave-wall stromatolite-like patinas from a deep-cave environment in Italy. Our multimethodological approach, integrating optical microscopy, SEM-EDS, μXRF, XRPD, FT-IR, and Raman spectroscopy results, allowed a proper phases identification, investigate the microscale spatial distribution of the different minerals, the oxidation state of Mn, microbial imprints, morphological features, and variation in the Mn/Fe ratio along the accumulation direction. A preliminary assessment of the microbial ecology was carried out through DNA sequencing of the uncultured prokaryotic community 16S rRNA gene pool. We used this large multimethodological dataset to explore the significance of MnFe-deposits as paleohydrological indicators.

GEOLOGICAL SETTING OF THE STUDY AREA

The studied samples of MnFe patinas were collected in the *Grotta del Cervo* cave (also known as *Grotta Grande dei Cervi*) (Central Italy, Carsoli, L'Aquila, see **Figure 1** and **Supplementary Figure S1**). The cave, with the nearby sinking stream *Grotta dell'Ovito di Pietrasecca* and spring *Risorgenza di Vena Cionca* (**Figure 1**), is part of the Pietrasecca karst system, which hosts one of the most typical "through caves" in the Central Apennines. In particular, the *Grotta del Cervo* cave represents the paleosink of the karst system, which is now active with the *Grotta dell'Ovito di Pietrasecca* (Agostini and Piccini, 1994). The cave entrance is located at 42°08′09.136″ N, 13°07′ 43.558″ E, at an altitude of 858 m above sea level. The cave system has an overall height difference of 107 m (+6/−113 m) and a development of 1875 m.

The Pietrasecca karst system is located in the central portion of the Carseolani Mts. (Central Apennines), about 50 km NE of Rome. This area is characterized by pre-orogenic Meso-Cenozoic shallow-water carbonates, belonging to the Latium-Abruzzi carbonate platform (limestones with rudists, and limestones with bryozoa and red algae), which are overlain by Late Miocene synorogenic deposits related to an Apennine foredeep basin (Orbulina marls, and Argilloso-arenacea Fm.) (**Figure 1**) (Cosentino et al., 1997, and references therein). This portion of the Carseolani Mts., trending from NW to SE, is bounded by a set of faults trending NE-SW (Agostini and Piccini, 1994). The caves are developed along some sets of fractures, transversally to the ridge, and they are prevalently vadose in their morphologies. They show a strong erosive activity linked to high water flow associated with high solid transport (Agostini and Piccini, 1994). Seismic activity controlled the evolution of the Pietrasecca karst system during the last 350 Ky (Postpischl et al., 1991). Earthquakes caused changes in the groundwater circulation and physicochemical conditions, which affect the color,

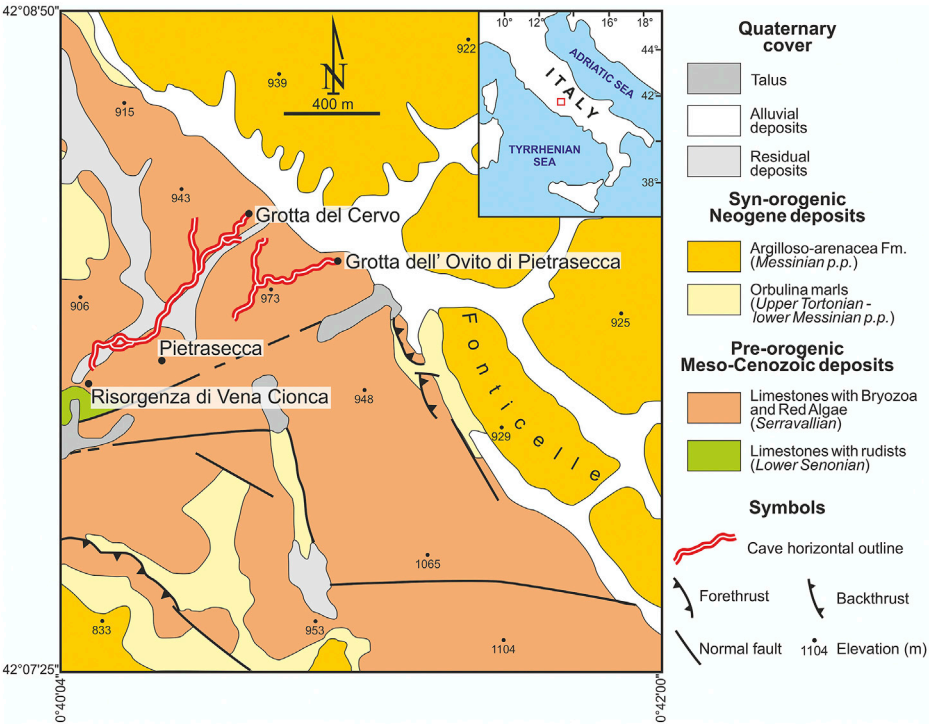

FIGURE 1 | Geological map of the study area, redrawn from Cosentino et al. (1997).

crystallinity, mineralogy, and textural features of carbonate speleothems. For instance, the last generation of carbonate speleothems in the *Grotta del Cervo* started growing after the December 1456 earthquake (the largest historical known earthquake occurred in peninsular Italy) (Postpischl et al., 1991). Black MnFe patinas are widespread in the deepest and active cave section (Forti, 1994), characterized by a strong ancient erosive activity. These patinas are occasionally submerged today by the increase of the underground river level during flooding, but only in response to periods of heavy rain. MnFe deposits can also be observed inside the *Grotta dell'Ovito di Pietrasecca,* and in general, where the hydrogeological and morphological conditions are similar to those of the deepest section of the *Grotta del Cervo*.

SAMPLE COLLECTION AND EXPERIMENTAL METHODS

Black patinas coat the walls of *Grotta del Cervo*, especially in the presence of streams and water pools. A total of six samples were collected from the patinas covering the walls of the cave, in the section of the cave named "*Fiume di Fango*", 1 km from the entrance and at an altitude of ca. 810 m asl, about 1 m above the water level (see **Supplementary Figures S1, S2**). In this area, characterized by mud on the floor, the patinas are continuous black coatings that extend from a few tens of centimeters to a few meters above the average water level. These mineralizations occur more frequently as patchy coatings on the areas sheltered from the water current by the irregularities of the walls (scallops, solution pockets, pendants, and echinoliths). In this part of the cave, the pH of water is 7.1, temperature is nearly constant throughout the year (~8 °C) with relative humidity close to saturation (97.7%). For biological analysis, five replications of the black patinas were scraped off the mud coating, and collected in sterile tubes containing RNAlater and kept in cold storage until the arrival in the laboratory, then stored at -80°C. Another sample (named GC), about 3 mm thick, consisting of black layers and brown lenses (**Figure 2**), was also collected for mineralogical and elemental characterizations (see **Supplementary Figure S2**). For this purpose, a polished cross-section (prepared by impregnating the sample with epoxy resin to maintain its integrity during the polishing operation) was used for punctual SEM-EDS, μXRF, and Raman analyses (**Figure 2**). Finally, material from a black layer (GC1) and a brown detrital lens (GC2) (see **Figure 2** for the position on the sample) was carefully extracted by hand-picking (particular care was taken to avoid getting materials from other layers) and grounded to powder for whole-rock XRPD and FT-IR analyses.

SEM analyses were carried out at the *Laboratorio Interdipartimentale di Microscopia Elettronica* (LIME), Roma Tre University, using a Zeiss Sigma 300 FE-SEM (Field-Emission Scanning Electron Microscope). The microscope is equipped with a HDBSE (High Definition Back Scatter Electron) detector and an energy dispersive (EDS) Bruker QUANTAX detector. The elemental composition was determined using an accelerating voltage of 20 kV, a filament current of 1.80 A and an aperture size of 20 μm. High-pass filtering of the SEM images collected along the growth of the

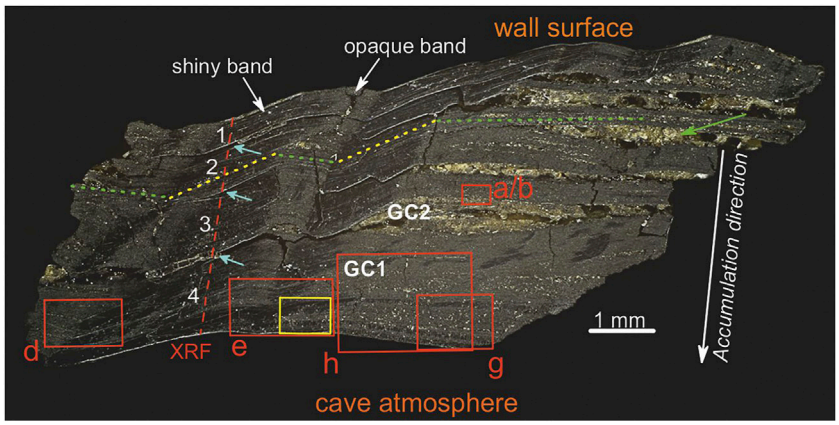

FIGURE 2 | Optical microscope image of the polished cross-section (sample GC). Red boxes indicate the areas investigated by SEM-EDS (**Figure 4**), while the yellow box indicates the position of Raman map (**Figure 7**). Red dashed line indicates the μXRF scan profile (**Figure 9**). Green and yellow dotted lines show the layer orientations (horizontal and transversal, respectively). Cyan arrows indicate discontinuous surfaces between the black layers (numbered in white). The green arrow indicates a detrital lens. GC1 and GC2 show the areas selected to extract the material for XRPD and FT-IR.

patinas was used to sharpen and count the micro-laminae (~1.5 μm thick) and laminae (~5–20 μm thick) within the sample.

X-Ray Powder Diffraction (XRPD) was performed at the *Laboratorio di Diffrazione ai Raggi X*, Department of Science, Roma Tre University, using a Scintag X1 diffractometer under CuKα1 radiation (λ = 1.54055 Å, 40 mA, 45 kV), fixed divergence slits and a Peltier-cooled Si(Li) detector (resolution < 200 eV). A divergent slit width of 2 mm and a scatter-slit width of 4 mm were employed for the incoming beam; a receiving slit width of 0.5 mm and scatter-slit width of 0.2 mm were used for the diffracted beam. Data were collected in step-scan mode in the 5–70° 2θ range, with a step size of 0.05° 2θ, and a counting time of 3 s/step.

Powder Fourier Transform Infrared Spectroscopy (FT-IR) data were collected at the *Laboratorio di Spettroscopia Infrarossa*, Department of Science, Roma Tre University, using a Nicolet iS50 FTIR spectrometer equipped with a DTGS detector and a KBr beamsplitter; the nominal resolution was 4 cm^{-1}, and 64 scans were averaged for each sample and for the background. Samples were prepared as pellets containing about 1 mg of powdered sample in 200 mg of KBr.

Raman measurements were performed at the *Laboratorio di Spettroscopia Raman*, Department of Science, Roma Tre University, at room temperature using an inVia Renishaw Raman spectrometer equipped with a diode laser (532 nm, output power 50 mW), an edge filter to select the Raman scattering avoiding the elastic contribution, a 1800 lines per mm diffraction grating and a Peltier cooled 1,024 x 256 pixel CCD detector. Samples were mounted on the manual stage of a Leica DM2700 M confocal microscope. Focusing of the laser beam and collection of Raman signals were obtained with a 50x long-working distance objective. Following Bernardini et al. (2019, 2020b) Raman spectra were collected by keeping the laser power on the sample at 1 mW, thanks to the use of neutral filters, and each accumulation time was fixed at 10 s to avoid any possible laser-induced degradation of the sample. Raman mapping was carried out on a polished cross-section, by collecting a grid of single-point spectra, at 50 × 30 μm step, for a total number of 89 points, from 200 to 900 cm^{-1}. Following Bernardini et al. (2020a) the intensity ratio between the band around 630 cm^{-1} (assigned to the ν_1 stretching mode of Mn^{4+}-octahedra) and the band around 570 cm^{-1} (assigned to the ν_1 stretching mode of Mn^{3+}-octahedra) was integrated over the scanned area to map the spatial distribution of the oxidation state of Mn. The Raman spectrometer was calibrated prior to the measurements using a Si wafer and by performing the automatic offset correction. The spectra acquisition and data analyses were accomplished using WiRE™ and Origin 9.0 software. The peak positions are estimated to be accurate to at least ±2 cm^{-1}.

Micro X-ray Fluorescence (μXRF) was performed at the XRF beamline of the Brazilian Synchrotron Light Laboratory (LNLS, Campinas, Brazil) to study the distribution of elements. Measurements were acquired at 10 keV along a 3.125 mm scan-line profile, orthogonally to the growth of the mineralization (see **Figure 2** for the location), at 25 μm step for a total number of 125 points, and count time per point of 600 ms. The softwares PyMCA 5.4.2 and Origin 9.0 were used for spectra calibration and processing, and for data elaboration, respectively.

The polished cross-section (**Figure 2**) was also investigated for the presence of microbial imprints by a Zeiss Gemini500 SEM of *Centro Microscopie* of the University of L'Aquila. Micrographs were acquired working with variable pressure and using an acceleration voltage of 10 kV and with a BSD4 detector (to detect backscattered electrons).

DNA extraction was performed two times on 0.5 g of homogeneous samples of black patinas (5 sub-samples mixed) fixed in RNA-later by a NucleoSpin® Soil kit" (Macherey Nagel, Germany). DNA extraction was performed following the manufacturer's protocol. The extracted DNA samples (named GCA and GCB) were sent to Bio-Fab Research laboratories (Italy) for purification and sequencing. The amplification of prokaryotes (bacteria and archaea) was obtained by a specific protocol of the

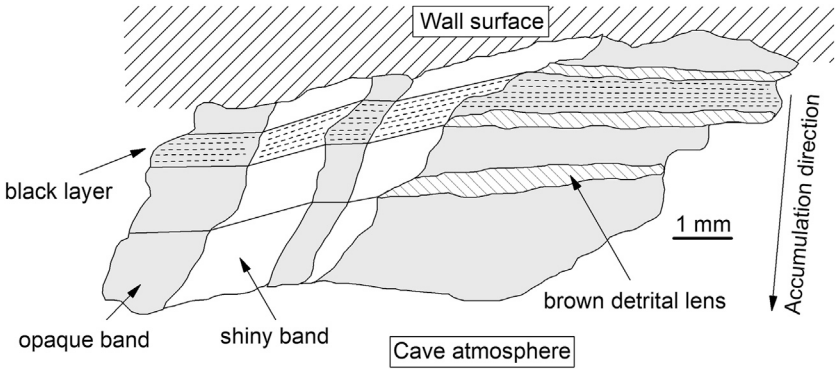

FIGURE 3 | Sketch of the sample GC showing the brown detrital lenses, black layers, and the lateral alternation of shiny (white colour) and opaque (gray) bands. The dashed lines show the orientation of the layering within the opaque and shiny bands (horizontal and transversal, respectively).

Mi-Seq Illumina platform, using primers that targeted the V3 and V4 regions of 16S rRNA – i.e. Forward Primer = 5′ TCGTCGGCAGCGTCAGATGTGTATAAGAGACAGCCTAC GGGNGGCWGCAG, Reverse Primer = 5′ GTCTCGTGGGCTCGGAGATGTGTATAAGAGACAGGACT ACHVGGGTATCTAATCC (Choi et al., 2020). A metagenomic workflow was carried out to classify microorganisms, using QIIME2 (Bolyen et al., 2019) and SILVA 132 database (https://www.arb-silva.de/); taxonomic assignments were checked through LPSN service (https://lpsn.dsmz.de). The Shannon Index (H′) and rarefaction curves were obtained by PAST 4.03 software (Hammer et al., 2001).

RESULTS

Elemental Composition and Mineralogy

A careful optical microscope study of the cross-section revealed a layered texture made of millimetric black layers and brown lenses (**Figure 2**). Brown lenses (green arrow in **Figure 2**), with a thickness of ~ 0.3 mm, are made of micrometric crystals/grains of detrital minerals, such as quartz, feldspar, and phyllosilicate-like minerals. All the brown lenses show the same horizontal orientation (green dotted line in **Figure 2**). Black layers consist of micrometric detrital crystals/grains embedded in a fine black matrix. Four layers, with an average thickness of ~ 0.7 mm, were identified (white numbers in **Figure 2**). These layers are separated by discontinuity surfaces (indicated by cyan arrows in **Figure 2**), with lateral transition into the brown detrital lenses (to the right in **Figure 2**). Moreover, "opaque" and "shiny" bands (due to the occurrence of materials with different mechanical properties, less resistance to polishing for the former), characterized by a different strata orientation were identified. The layering within the opaque bands is horizontally orientated (*i.e.,* the same orientation of the brown detrital lenses, green dotted line in **Figure 2**). Moreover, these bands are associated with detrital minerals but with a smaller size than the minerals within the brown lenses, while the layering within the shiny bands is transversely oriented (yellow dotted line in **Figure 2**). As a result, opaque and shiny bands alternate laterally following the orientation of the layers, therefore following the geometry, *i.e.,* roughness, of the wall surface (the wall surface is not perfectly plane but is irregular and carved by concave and convex forms. Accordingly, the strata of the MnOx deposit have to follow and adjust to the geometry and roughness of the rock substratum, see **Figure 2** and **Figure 3**).

SEM-EDS analyses allowed us to define further the brown lenses, the black layers, and the shiny and opaque structures inside the latter based on their elemental composition and morphologies. The brown detrital lenses mainly consist of micrometric crystals of quartz and K/Mg-rich phyllosilicate-like minerals preferentially oriented parallel to the stratification (**Figure 4A**). Other phases, such as alkali-feldspar, Fe- and Ti-oxide(s) with minor zircon, pyroxene, and olivine (the latter probably related to the weathering of volcanic rocks outcropping inside the cave, see Bertolani et al., 1994; Stoppa et al., 2002) were also identified. Fe is ubiquitously present, while Mn is scarce to absent in these Fe-rich brown detrital lenses (**Figure 4B**), and abundant in the Mn-rich black layers (**Figure 4C**). EDS data collected from the black layers show high content in Mn, Fe, Ca and a lower content in K, Ba, Mg, Al, Si, Cl, and P. SEM-EDS images confirm the presence of opaque bands (initially identified under the optical microscope, see **Figure 2** and **Figure 3**), associated with detrital minerals and voids, whereas the shiny bands contain few detrital minerals (see the Si distribution in **Figure 4D**). The lateral alternation of these bands (relative to the layer orientation) is recognizable even at micrometric scale (**Figures 4D–F**). The accumulation of detrital minerals, within the opaque bands, can lead to the formation of micrometric lenses of debris (white arrow in **Figure 4F**).

Stromatolite-like features are recognized exclusively within the Mn-rich black layers. We have distinguished three different morphotypes based on morphological and mineralogical characteristics, alternating laterally within the Mn-rich black layers (**Figures 4G,H**). In detail: 1) *branched columnar* morphotype, typical of the opaque bands characterized by voids and detrital minerals, with a convex-outward micro-lamination (**Figures 4I,J**); 2) *flat-laminated* morphotype,

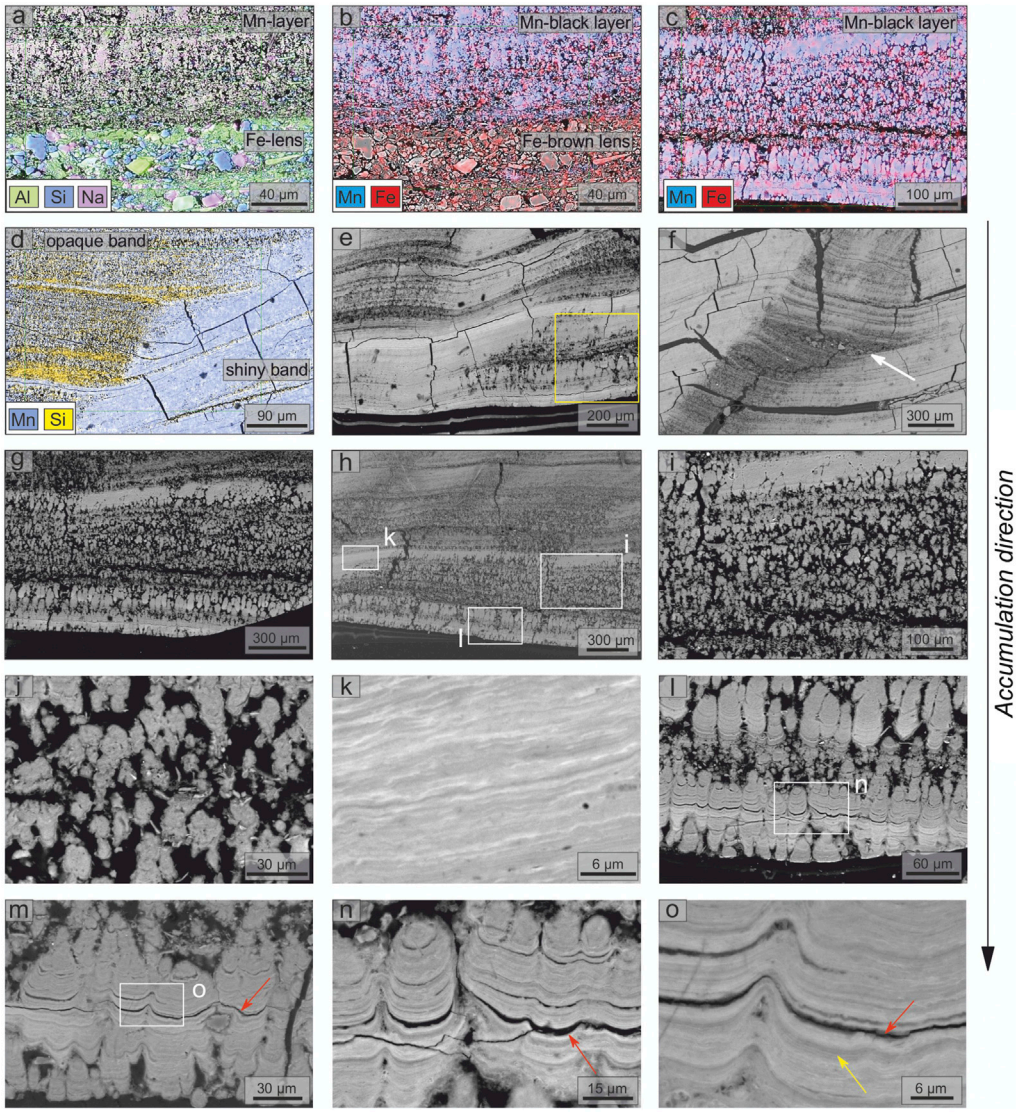

FIGURE 4 | SEM-EDS investigation of polished cross-section of the Fe-Mn patinas (sample GC): **(A, B)** EDS elemental maps (Mn, Fe, Al, Si, and Na) of the boundary between brown Fe-lens and black Mn-layer; **(C, D)** EDS elemental maps (Mn, Fe, and Si) of black Mn-layers; **(E, F)** alternation of the shiny and opaque bands, yellow box indicates the position of Raman map shown in **Figure 7**; **(G, H)** spatial distribution of the three different morphotypes identified, white boxes indicate the positions of panels **(I)**, **(K)**, and **(L)**; **(I, J)** detail of the *branched columnar* morphotype; **(K)** detail of the *flat-laminated* morphotype; **(L–O)** details of the *columnar or pseudo-columnar* morphotype (see **Figure 2** for the position on the sample). White arrow indicates a lens of debris. Red arrows indicate discontinuity between laminations. Yellow arrow shows ~1.5 µm bands.

characterized by flat and parallel micro-lamination (**Figure 4K**); and 3) *columnar or pseudo-columnar* morphotype, characterized by outward, dome-like structures (**Figures 4I–O**). Morphotypes 2) and 3) were recognized in the shiny bands only. Layering at different scales was identified throughout the sample, especially in the *flat-laminated* and *columnar or pseudo-columnar* morphotypes (**Figure 4**). Nano-laminae, with a thickness of hundreds of nanometers (**Figure 4O**), were identified. These nano-laminae form darker and lighter micro-laminae with a thickness of ~ 1.5 µm (yellow arrow in **Figure 4O**), which in turn form laminae (sometimes separated by discontinuity surfaces, red arrows in **Figures 4M–O**) with a variable thickness from 5 to 20 µm (the thicker ones are associated with detrital minerals). Nano-laminae, micro-laminae and laminae form super-laminae with a thickness of ~ 300–400 µm, which, in turn, form the four millimetric layers observed (see **Supplementary Figure S3** for details). Along the µXRF scan line profile (red dotted line in **Figure 2**), in areas belonging to the *flat-laminated* morphotype, a total of ~ 1900 micro-laminae, which form ~ 170 laminae, has been recognized.

Mineralogy of the brown detrital lenses and the black layers (GC2 and GC1 in **Figure 2**, respectively) is further elucidated through X-ray powder diffraction, FT-IR, and Raman spectroscopy.

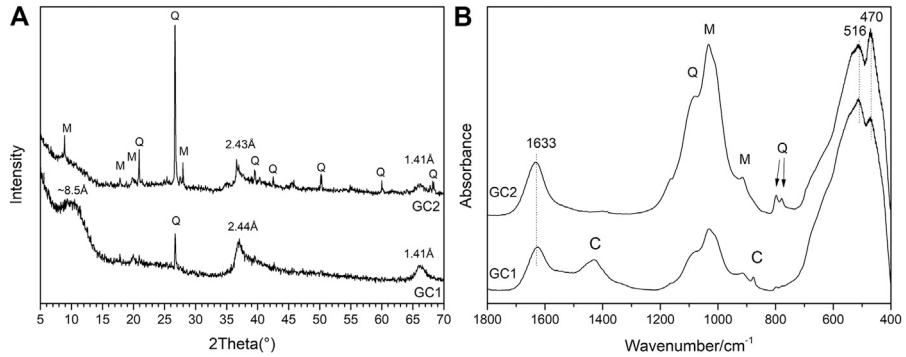

FIGURE 5 | XRPD **(A)** and FT-IR **(B)** results from the black layers (GC1) and brown layers (GC2) (**Figure 2** shows the areas selected to extract the material for the analyses). M, mica; Q, quartz, C: carbonate minerals.

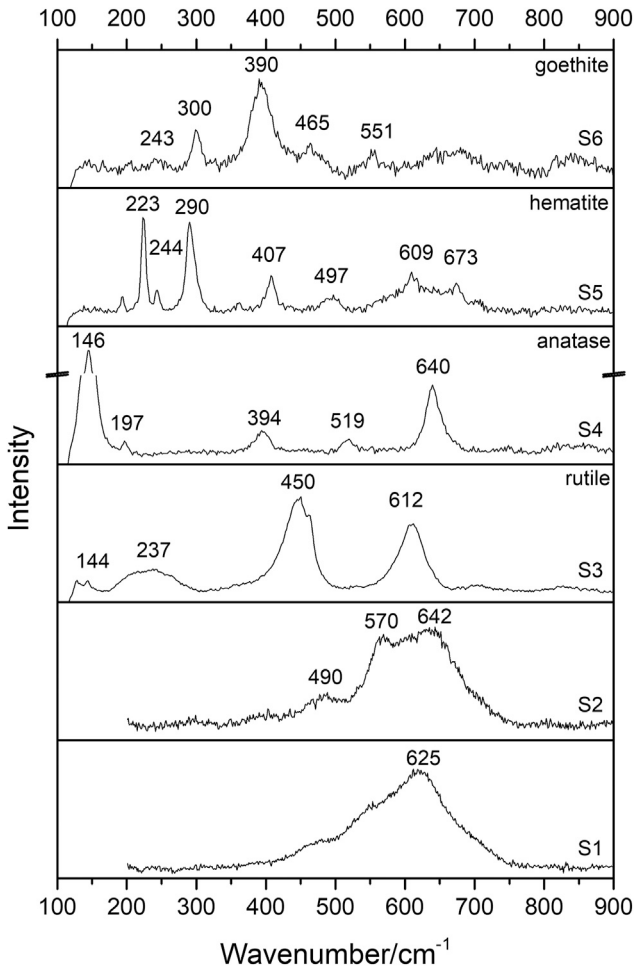

FIGURE 6 | | Raman spectra collected on black layers (spectra S1, and S2) and brown lenses (spectra S3, S4, S5, and S6). Spectra collected at λ = 532 nm.

X-ray powder diffraction data collected on the brown detrital lens (GC2 in **Figure 5A**) showed sharp Bragg peaks of quartz at *d-spacing* (Å)(I%) 4.26(20), 3.34(100), 2.28(5), 1.82(10), and mica (muscovite and/or phlogopite) at *d-spacing* (Å)(I%) 9.95(100), 4.99(30), 3.20(90). Broad peaks of poor-crystalline and/or nanocrystalline compounds were also detected. Strong peaks at 2.43 and 1.41 Å allow recognizing vernadite [$(Mn,Fe,Ca,Na)(O,OH)_2 \cdot nH_2O$], a disordered variety of

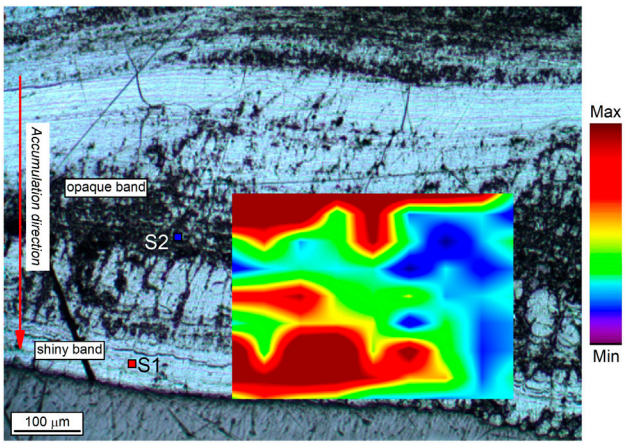

FIGURE 7 | Raman map of the oxidation state of Mn obtained by integrating the intensity ratio between the band at 630 cm^{-1} (ν_1 stretching mode of Mn^{4+}-octahedra) and the band at 570 cm^{-1} (ν_1 stretching mode of Mn^{3+}-octahedra) over the scanned area (see methods for details). Red/yellow: higher average oxidation state of Mn (todorokite and/or ranciéite in a shiny band), blue/green: lower average oxidation state of Mn (vernadite in an opaque band). S1 and S2 are the spots where Raman spectra of **Figure 6** were obtained.

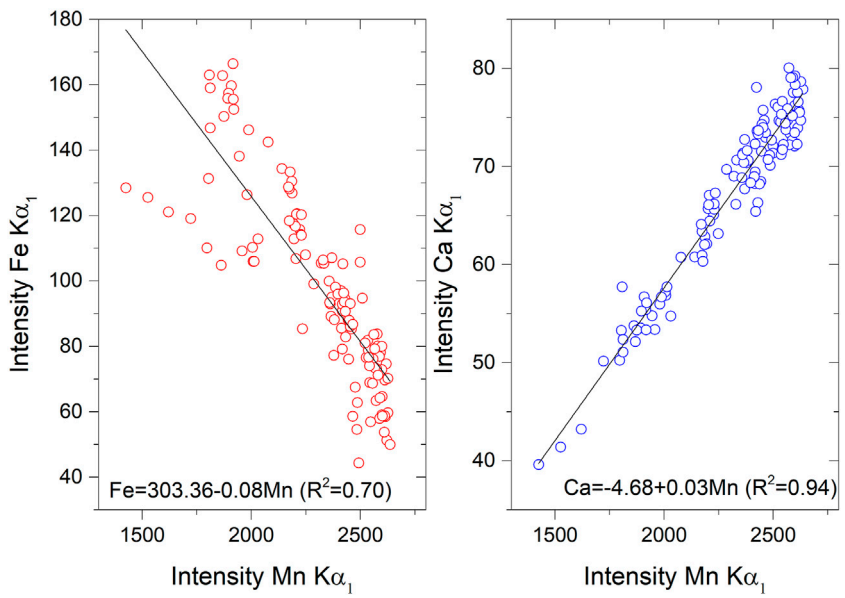

FIGURE 8 | Scatter plot of the abundances of Mn, Fe, and Ca measured along the µXRF scan profile (see **Figure 2**).

birnessite typical of crusts throughout the global ocean. Since SEM-EDS data show Mn is absent in these layers (**Figure 4B**), the presence of this Mn-phase in the sample is possibly due to the accidental collection of material from nearby layers. Diffraction data collected on the black Mn-layers (GC1 in **Figure 5A**) showed the strongest peaks of quartz and broad peaks of vernadite at 2.44 and 1.41 Å. Moreover, a very broad peak, centered around 8.5 Å, was also detected. This broad peak can be due to the 001 reflection of mica, clay minerals, and/or to the presence of poorly/nano crystalline 7Å (birnessite and ranciéite) and/or 10Å (buserite and todorokite) Mn-phases.

The same powdered samples previously used for XRPD were also investigated by FT-IR. The spectrum collected on the brown detrital lenses (GC2 in **Figure 5B**) shows strong and broad bands of silicates (*i.e.,* quartz and muscovite) around 1,000 cm^{-1}. While, the black layers (GC1 in **Figure 5B**) show weak absorptions bands of silicates and carbonates, the latter at 1,430 and 875 cm^{-1} (labelled as C in **Figure 5B**), due to the occurrence of carbonate traces not detectable by XRPD. Finally, both samples show broad and unresolved absorption bands at 470, 516, and 1,633 cm^{-1}, which point to the presence of highly disordered and/or nanocrystalline Mn-compounds. These bands can be assigned to

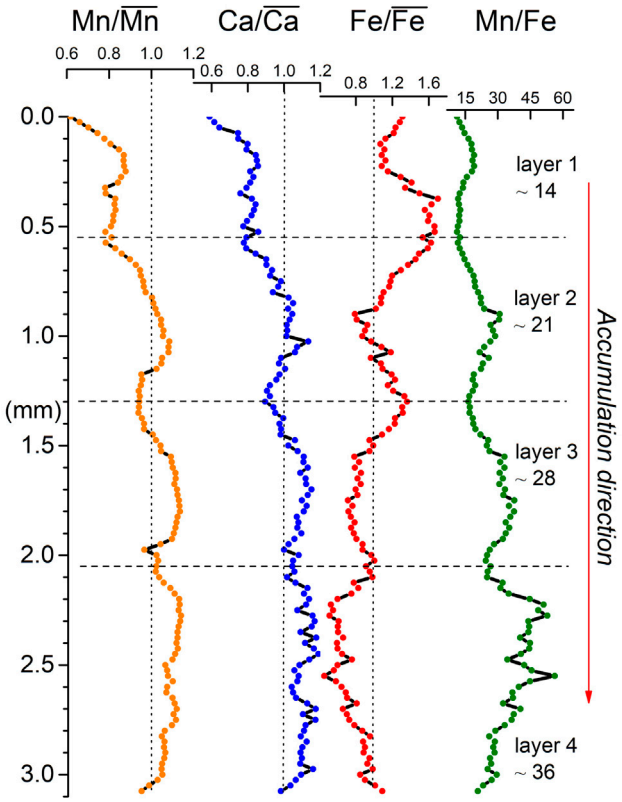

FIGURE 9 | Mn/$\overline{\text{Mn}}$, Fe/$\overline{\text{Fe}}$, Ca/$\overline{\text{Ca}}$, and Mn/Fe profiles along the growth direction of sample GC, obtained by μXRF (see **Figure 2** for the position on the sample). Horizontal dotted lines mark the boundary of each cycle (minimum Mn/Fe values) corresponding to the discontinuity surfaces between layers (cyan arrows in **Figure 2**).

several MnOx, such as birnessite, ranciéite, todorokite, and vernadite (Chukhrov et al., 1978; Potter and Rossman, 1979).

Raman spectra were collected in several points of the brown detrital lenses and the black layers to check for heterogeneities. Four different spectra were obtained from the brown detrital lenses (spectra S3 to S6 in **Figure 6**). Titanium dioxides, such as rutile (bands at 144, 237, 450 and 612 cm^{-1}, spectrum S3) and anatase (bands at 146, 197, 394, 519 and 640 cm^{-1}, spectrum S4) (Balachandran and Eror, 1982), and Fe oxides, such as hematite (bands at 223, 244, 290, 407, 497, 609 and 673 cm^{-1}, spectrum S5) and goethite (bands at 243, 300, 390, 465 and 551 cm^{-1}, spectrum S6) (de Faria and Lopes, 2007), were detected. Two different spectra were obtained from the Mn-rich black layers as follows: spectrum S1, collected on the shiny bands (*flat-laminated* and *columnar* or *pseudo-columnar* morphotypes, see **Figure 7** for the position of the spot in the sample), is characterized by a strong and broad band at ~ 625 cm^{-1} and shoulders at ~ 570 and 490 cm^{-1} (**Figure 6**). These spectral features can be assigned to ranciéite or todorokite (Bernardini et al., 2019). Moreover, also considering XRPD and FT-IR results, neither can be excluded. Spectrum S2, collected on the opaque and silicate/void-rich bands (*branched columnar* morphotype, see **Figure 7** for the position of the spot in the sample) is characterized by strong and broad bands at ~ 642 and 570 cm^{-1} and a weak band at ~ 490 cm^{-1} (**Figure 6**). According to XRPD and FT-IR results, this spectrum can be assigned to vernadite (Post et al., 2003). Bernardini et al. (2020a) calibrated a method to extract the oxidation state of Mn from the Raman spectra. Following this method, we show that Mn occurs as Mn^{4+} (recognized by the band at 625 or 642 cm^{-1}) and as Mn^{3+} (recognized by the band at 570 cm^{-1}) (see spectra S1 and S2 in **Figure 6**).

Following Bernardini et al. (2020a), the microscale spatial distribution of the Mn oxidation state at the boundary between an opaque and a shiny band was studied by Raman mapping (**Figure 7**). Opaque bands, associated with vernadite, silicate minerals, and voids (*branched columnar* morphotype), are characterized by a lower oxidation state of Mn (blue area in **Figure 7**). In contrast, shiny bands, associated with todorokite and/or ranciéite (*flat-laminated* and *columnar* morphotypes), are characterized by a higher oxidation state of Mn (red area in **Figure 7**).

XRF data were collected from the same area used to count the ~1.5 μm microlaminae and the ~10 μm laminae (*i.e.,* along a shiny band, see **Figure 2**), avoiding detrital crystals and voids. Consistently with EDS results, XRF data show high content of Mn, Fe, Ca, and smaller amounts of K, Ba, Ti, and P. Moreover, heavy metals, such as V, Ni, Zn, Cu, and As, were also detected.

A μXRF scan-line profile (see Methods and **Figure 2**) allows investigating the variations in elemental abundances along the accumulation direction of the patinas, and at the transitions between the four millimetric layers (white numbers in **Figure 2**). A positive correlation between Mn and Ca (R^2 = 0.94), suggests that the sample consists of Ca-rich MnOx. Moreover, Mn shows a negative correlation with Fe (R^2 = 0.70) (**Figure 8**).

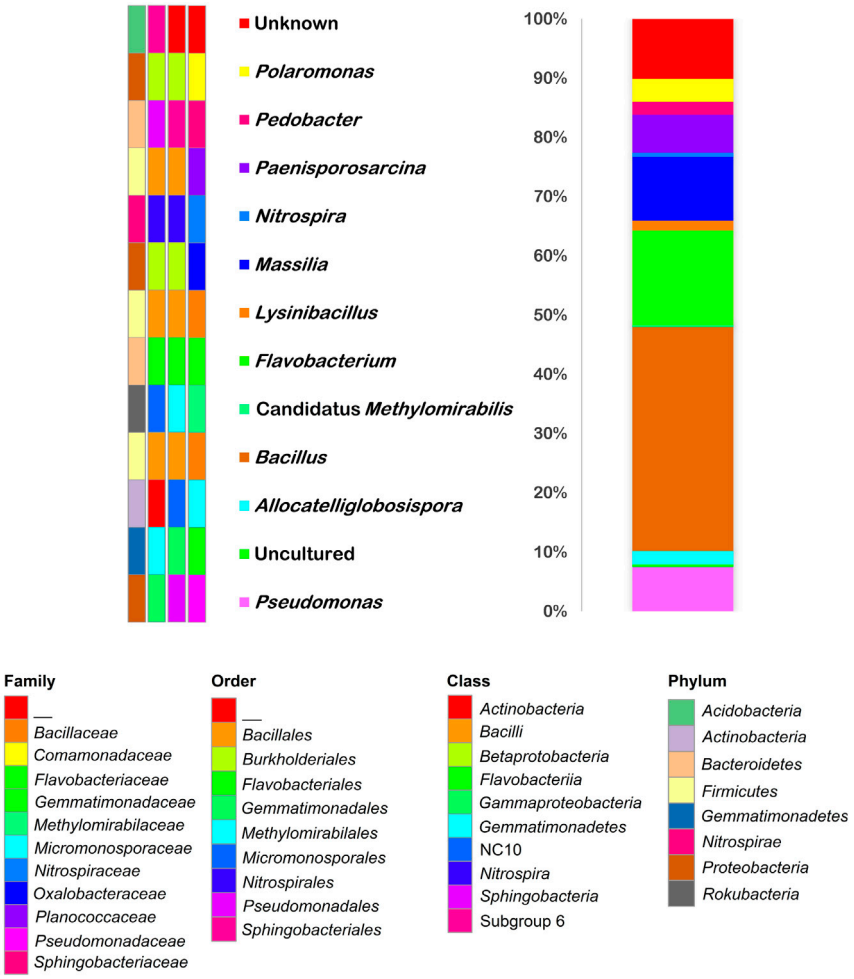

FIGURE 10 | Taxonomy barplot of microbial community composition of the Fe-Mn patina sample. The color changes in the barplot show the percentages occupied by genera (color keys on the left). Taxa assignments (P, phylum; C, class; O, order; F, family) are indicated by the color keys on the bottom.

μXRF profiles show four main oscillations for Mn, Fe, and Ca (**Figure 9**), each one related to one of the four millimetric layers. They can be recognized by Mn peaks (*i.e.,* max relative values) and Fe troughs (*i.e.,* min relative values) toward the center of the layers and Fe peaks and Mn troughs at the boundaries of the layers. The Ca pattern resembles that of Mn. Moreover, the oscillations are characterized by a trend in the Mn/Fe ratio, which increases from the older to the younger layers (i.e. from layer 1 to layer 4 in **Figure 2**). Mean Mn/Fe ratios increase from ~ 14 in cycle 1 (the oldest), to ~ 21 in cycle 2, 28 in cycle 3, and 36 in cycle 4 (the most recent). The minimum Mn/Fe values (black dotted horizontal line in **Figure 9**) are associated with the discontinuity surfaces (cyan arrows in **Figure 2**). The mean Mn/Fe ratio in the whole profile is ~ 26 (min ~ 11 and max ~ 55).

Microbiological Analysis

The Illumina sequencing results on GCA and GCB samples showed very similar profiles. Thus, we considered the combined profile for further elaborations. The single GCA and GCB samples profiles at the genus level, the quantitative reports of sequencing and metagenomic analysis, the calculated Shannon Index (H′), and diversity rarefaction curves are shown in **Supplementary Material** (**Supplementary Figure S3** and **Supplementary Table S5**). The results showed that the investigated samples have high diversity (H' > 3; GCA: 4.76 and GCB: 5.91) and that the communities are mainly composed of *Bacteria* (~99%), with a very small percentage of *Archaea* (~1%). Within the *Archaea* domain, except for the identified phylum *Bathyarchaeota* with a relative abundance of 2.4%, an unknown taxon was found. Within the *Bacteria* domain, the predominant phyla (**Supplementary Table S1**) were *Firmicutes* (36%), *Proteobacteria* (33%), and *Bacteroidetes* (13%). Another phylum with a significant relative abundance was *Actinobacteria* (7%). Less abundant phyla were *Acidobacteria, Chloroflexi*, and *Planctomycetes* (relative abundances over 2%). The distribution in classes of the different phyla (**Supplementary Table S2**) showed that the most abundant class was *Bacilli* (35%), followed by *Betaproteobacteria* and *Flavobacteria* (18 and 12%,

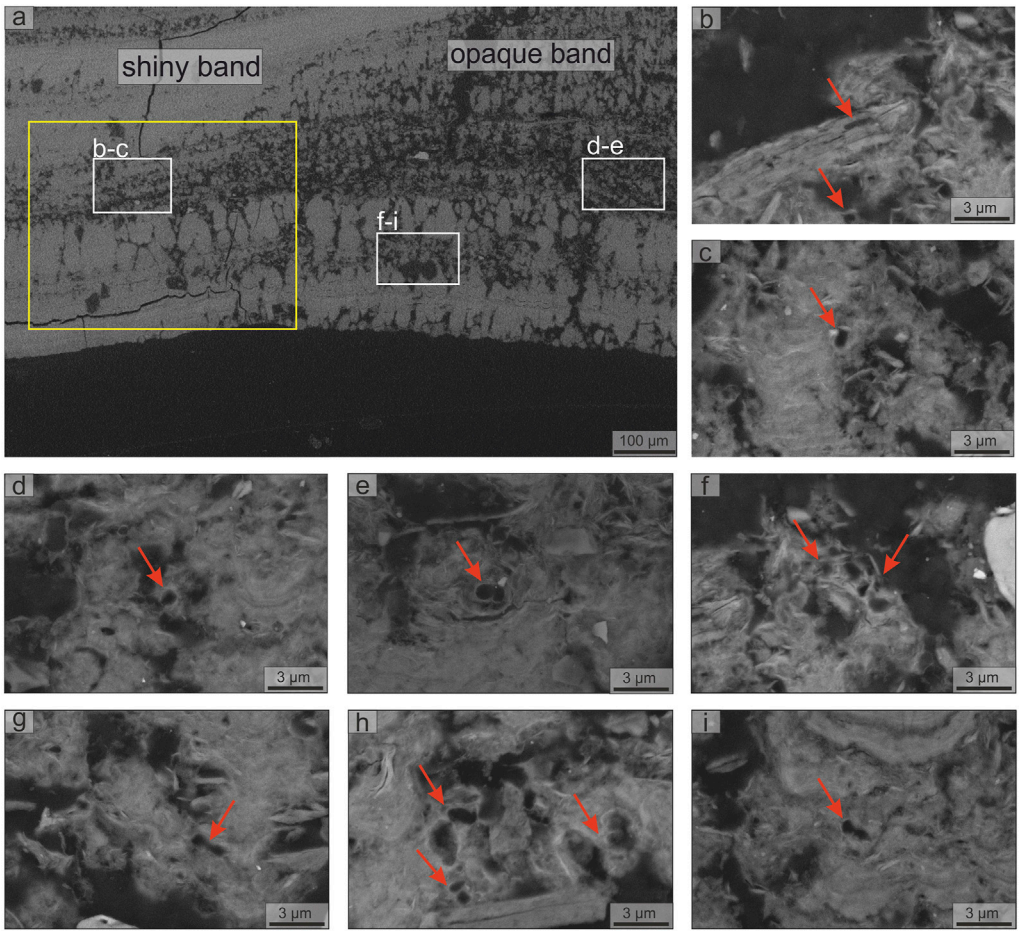

FIGURE 11 | SEM-EDS investigation of polished cross-section of the Fe-Mn patinas (sample GC): **(A)** areas of investigation, white boxes indicate the positions of other panels, yellow box indicate the position of the Raman map (**Figure 7**), **(B–I)** bacterial microbial imprint (red arrows). Putative predivisional cell stages typical of staked bacteria are showed in panels **(E)**, **(G)**, and **(I)**.

respectively). Less abundant were *Alphaproteobacteria, Gammaproteobacteria*, and *Actinobacteria* classes (relative abundances over 4%). *Bacillales, Burkholderiales*, and *Flavobacteriales* were the main orders (35%, 15%, and 12%, respectively, **Supplementary Table S3**); while, among families, *Bacillaceae* and *Flavobacteriaceae* accounted for significant percentages (28 and 12%, respectively, **Supplementary Table S4**). In **Figure 10** the results of the relative abundances obtained for the genera and their taxonomic assignments are summarized. *Bacillus* (25%) was the predominant genus, followed by unknown and uncultured genera (18 and 17%, respectively). The remaining percentage was represented by other genera with a relative abundance ≤ 10%.

SEM images collected in the area previously investigated by Raman mapping (yellow box in **Figure 11A**) revealed the presence of empty bacterial sheath imprints (**Figures 11B–I**). Some of the latter can be identified as putative predivisional cells, typical of dimorphic prosthecate bacteria (**Figures 11E,G,I**). Moreover, we found an interesting spatial distribution of these imprints. They were identified only in areas with a lower oxidation state of Mn and detrital minerals (*i.e.,* opaque bands in **Figure 11A**). On the contrary, no evidence of microbial imprints was recognized in areas with a higher oxidation state of Mn (*i.e.,* shiny bands in **Figure 11A**).

A summary of the results obtained on the black layer (shiny and opaque bands) and brown lenses in sample GC is given in **Table 1**.

DISCUSSION

Mineralogical and Microbiological Implications

Our mineralogical and elemental characterization shows that the black patinas covering the walls of the *Grotta del Cervo* consist of brown detrital Fe-rich lenses and black Mn-rich layers. The former consisting of a fine-grained mixture of quartz, mica, titanium dioxides (anatase and rutile), zircon, and Fe oxyhydroxides, such as goethite and hematite. Instead, the latter consists of few detrital minerals embedded in a fine Mn-

TABLE 1 | Distribution of the mineralogy, oxidation state of Mn, stromatolite-like structures, and bacterial imprints between the black layers (shiny and opaque bands) and brown lenses, obtained integrating SEM-EDS, XRPD, FT-IR, and Raman spectroscopy results.

Sample GC		Mn, Fe, Ca minerals	Oxidation state of Mn	Detrital minerals	Stromatolite morphotypes	Bacterial imprints
Black layers (GC1)	shiny bands	todorokite/ranciéite, carbonates	higher	quartz, mica, anatase, rutile, zircon, pyroxene, olivine	flat-laminated and columnar	absent
	opaque bands	vernadite, carbonates	lower		branched columnar	present
Brown lenses (GC2)		hematite, goethite	/		absent	absent

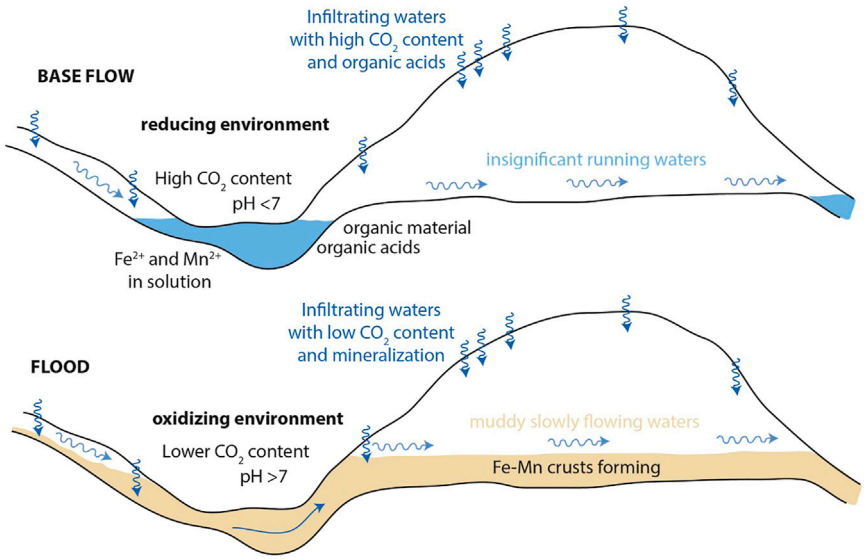

FIGURE 12 | Depositional model proposed for the MnFe patinas. During base flow hydrological conditions (upper panel), the studied karst system drains infiltrating water with no significant increase of underground water level. Patinas form during recurrent floods according to hydrological-driven changes on geochemical parameters and depositional conditions as explained within the text.

matrix. In these layers, the absence of Fe-oxides revealed by XRPD, FT-IR, and Raman spectroscopy, the negative correlation between Mn and Fe shown by μXRF data, and the necessity for balancing the entry of additional cations (such as Ca^{2+}) within the channel/interlayer sites, all suggest that Fe replaces Mn in the structure of Ca-rich MnOx. Our data show the occurrence of different MnOx, such as vernadite [$(Mn,Fe,Ca,Na)(O,OH)_2{\cdot}nH_2O$], a nano-sized or z-disordered variety of birnessite (Lee et al., 2019), and todorokite [$(Ca,Na,K)(Mn^{4+},Mn^{3+})_6O_{12}{\cdot}nH_2O$], a compound whose structure consists of triple chains of edge-sharing (Mn^{4+},Mn^{3+})O_6 octahedra linked such as to give channels with cross sections of 3x3 occupied by water molecules and large cations (Post and Bish, 1988; Post et al., 2003). Moreover, we cannot exclude the presence of ranciéite [$(Ca,Mn^{2+},K,Ba)(Mn^{4+},Mn^{3+})_4O_9{\cdot}nH_2O$], a phyllomanganate with disordered stacked layers of (Mn^{4+},Mn^{3+})O_6 octahedra, with water molecules and large cations located between the layers (Ertl et al., 2005).

An interesting aspect emerging from our microbiological investigation is the scarce contribution of *Archaea* to microbial communities. Most of the microbial communities of caves, located in different geographical regions and environmental conditions, showed an almost exclusive dominance of *Bacteria* and a negligible percentage of *Archaea* (Pasic et al., 2010; Itcus et al., 2018; Wiseschart et al., 2019; Jurado et al., 2020; Gonzalez-Pimentel et al., 2021). Only in a few cases, *Archaea* were linked to MnFe deposits, such as in Lechuguilla Cave (Northup et al., 2003).

Regarding *Bacteria*, the genera *Bacillus, Flavobacterium* and *Pseudomonas* represented almost 45% of the total relative abundance of the sample. *Bacillus* and *Pseudomonas* have been thoroughly investigated as model Mn-oxidizing bacteria (Francis and Tebo, 2002; Tebo et al., 2005; Jiang et al., 2010). Indeed, *Bacillus* spp. can remove Mn and other heavy metals due to their biosorption ability (Xu et al., 2019). The genus *Flavobacterium* was commonly detected in Mn deposits and Mn removal biofilters (Hou et al., 2020). *Flavobacterium* was also a member of the microbial communities inhabiting a birnessite-type Mn deposit in a Swedish mine (Sjöberg et al., 2018) and the Mn-oxidizing bacteria forming a biofilm in water transmission pipelines (Allward et al., 2018). Carmichael et al. (2013b) demonstrated the contribution of

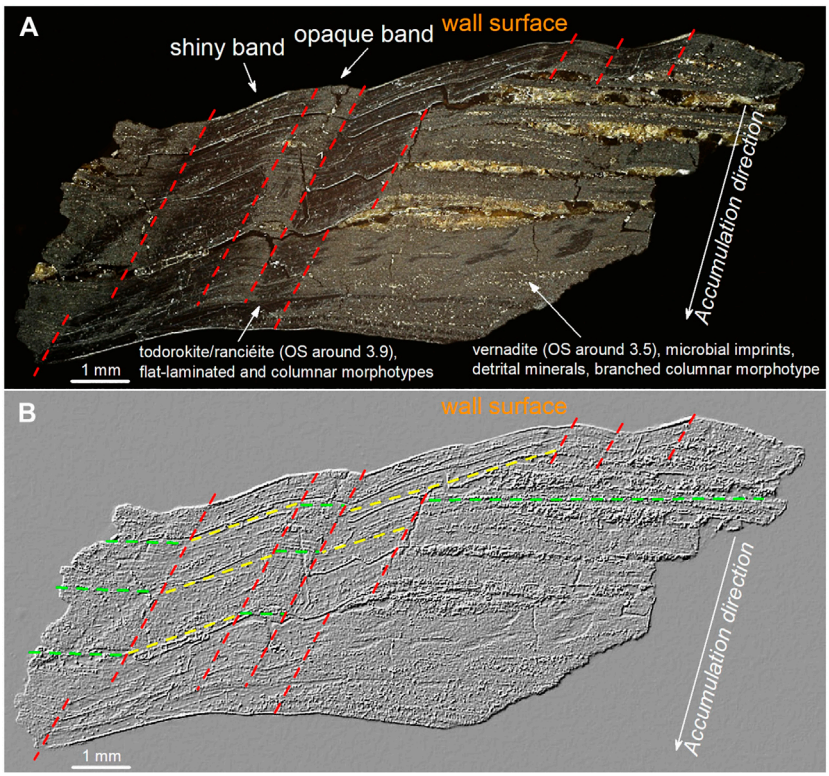

FIGURE 13 | Optical microscope image of sample GC **(A)**, and after directional filtering for linear enhancement **(B)**. These images show the distribution of shiny bands (associated whit layers transversely oriented, todorokite/ranciéite (OS ~ 3.9), and planar forms produced in a more turbulent "local" environment) and opaque bands (associated with layers horizontally oriented, vernadite (OS ~ 3.5), microbial imprints, detrital minerals, and forms produced in a less turbulent "local" environment, allowing the microbial community to stay attached to the wall surface). These bands alternate laterally, decreasing in number (from 7 to 2) along the accumulation direction of the patinas, as the surface becomes flatter. All the features point to strong control of the wall surface geometry (*i.e.,* roughness) on the spatial distribution of morphology, detrital mineral abundance, mineralogy of MnOx, and oxidation state of Mn. OS: average oxidation state of Mn.

Flavobacterium in the formation of cave MnFe deposits in the upper Tennessee River Basin by Mn(II)-biomineralizing bacteria isolation. Other less common bacteria involved in the biogeochemistry of Mn are found in the patinas of *Grotta del Cervo*. In fact, *Lysinibacillus* spp. were isolated from a Mn mining soil (Liu et al., 2013) and a Brazilian Mn mine (Barboza et al., 2015), and were able to solubilize low grade ores from a Mn deposit (Ghosh et al., 2016). Chen et al. (2019) isolated the Mn-oxidizing bacterium *Massilia* sp. from soil Mn nodules. He et al. (2008) stated that *Gemmatimonadetes* and *Nitrospirae* phyla occurred in acidic soil Mn nodules. Chaput et al. (2015) reported that microbial communities from Mn remediation systems, treating coal mine drainage, were composed of *Betaproteobacteria* mostly represented by the orders *Burkholderiales* and *Nitrosomonadales*, both of which have been found in the cave patinas.

Concerning the nature of the MnOx, *Bacillus* and *Pseudomonas* strains produced a poorly crystalline birnessite-like phyllomanganate (vernadite) that often represents the initial phase precipitated by bacteria during microbially mediated Mn^{2+} oxidation (Villalobos et al., 2003; Bargar et al., 2005). However, Feng et al. (2010) found that a strain of *Pseudomonas putida* formed nano-crystalline todorokite, and Kim et al. (2003) reported that *Leptothrix discophora* produced nanocrystalline todorokite-like manganese oxides. In this context, our microbiological data suggest that the genera identified in the samples could play a role in the Mn geochemical cycle. Moreover, our results show microbial imprints, some identified as putative predivisional cells (this fact has already been reported from other Mn deposits of *Grotta del Cervo, see* Vaccarelli et al., 2021), associated only with vernadite, suggesting a microbial origin for this highly disordered compound. In addition, bacteria of the genera *Bacillus, Flavobacterium*, *Pseudomonas*, *Lysinibacillus*, etc., appeared to be involved in calcium carbonate precipitation (Meier et al., 2017; Farrugia et al., 2019; Ortega-Villamagua et al., 2020). Most of these bacteria are ureolytic strains (Mitchell et al., 2019; Reeksting et al., 2020), although non-ureolytic precipitation was reported (Lee et al., 2017). Therefore, the bacteria identified in the manganese patinas have a high potential for biomineralization.

Hypothesis on the Hydrological Controls Driving MnFe Patina Formation

We here present a preliminary genetic model for the studied deposits (**Figure 12**), supposing that different karst hydrological

regimes lead to changes on cave geochemical environment and depositional conditions. Direct observations cannot be done during floods since the cave is inaccessible during these high flow conditions. Nevertheless, cave floods are here considered the main driver of the deposition of the patinas because of: 1) their location (*i.e.,* cave walls), 2) their morphological, sedimentological and mineralogical features, and 3) similar deposits described elsewhere (Rossi et al., 2010; Gázquez et al., 2011). Periods of intense rainfall would recharge the karst aquifer rapidly, increasing the water level up to a certain height according to the ratio between the water amount and drainage capability, as can occur in stream-passage caves (Columbu et al., 2015). During base flow hydrological conditions, the studied karst system drains infiltrating water with no significant increase of underground water level (**Figure 12**). However, floods are recurrent in this area, generally during autumn (rain events) and spring (snowmelt season). Water entrains detrital grains during floods; the mud deposits, well recognizable on the explored cave floors and walls (**Supplementary Figure S2**), witness this process. Recent mud deposits show a soft texture (*i.e.,* unconsolidated), confirming that flooding processes are still active in the *Grotta del Cervo* Cave (as reported by cavers). However, the studied patinas are consolidated, and they are found stratigraphically below the soft mud deposits (**Supplementary Figure S2**). From a geochemical perspective, the clear separation between Mn and Fe found in the sample may be due to variations in the redox conditions of the system. In fact, compared to Fe-oxides, MnOx are stable only under basic conditions (pH > 8), except at high oxidation/reduction potential (Eh > 600 mV) (Hem, 1963, 1972). In accordance, the MnFe patinas are deposited during the subaqueous period in the oxidizing environment when flood is rising, with Mn depositing first and Fe, together with detrital particles, in the later dewatered stage (when pH falls back to neutral or turns slightly acidic). When flood water retreats, slow decantation leaves the clay particles settle down slowly, covering the patinas again. The latter constitutes the unconsolidated deposits still visible in the studied cave. Thus, MnFe patinas can be considered indicators of cave paleo-flooding, with more basic conditions during the floods peaks (thus promoting an oxic geochemical environment), and less basic conditions during the flooding increases and decreases (thus promoting a sub-oxic geochemical environment). Accordingly, a cyclical shift between oxic (high Mn/Fe ratio) and suboxic (low Mn/Fe ratio) conditions, related to flood rise and retreat, may have led to the formation of Mn-layers or Fe-lenses and oscillations of the Mn/Fe ratio along the accumulation direction of the patinas. Because more recent floods did not erode patinas, it is reasonable to think that during flooding, in this part of the cave, the water rises and falls gently, without causing turbulent flow. In the rising flood period, waters can flow slowly through the cave passages, possibly only cleaning the walls from the more recent unconsolidated soft mud coatings left by previous floods.

Significance of Patinas Morphotypes

Black Mn-layers show bands, developed along the accumulation direction of the patinas, characterized by different appearance (shiny or opaque), relative orientation of the layering, mineralogy, microbial imprints, and stromatolite-like structures (**Figure 13**). In these areas three morphotypes were identified: 1) *branched columnar* morphotype (**Figures 4I,J**). This morphotype, typical of opaque bands (**Figure 13**), is associated with vernadite, microbial imprints, detrital minerals, and voids. Moreover, it occurs exclusively within layers displaying the same orientation of the Fe-lenses (green dotted lines in **Figure 13B**). While 2) *flat-laminated* morphotype (**Figure 4K**) and 3) *columnar or pseudo-columnar* morphotype (**Figures 4I–O**) are typical of the shiny bands (**Figure 13**). These latter two morphotypes are associated with todorokite and/or ranciéite, with a lower detrital mineral content, and occur exclusively within layers displaying an orientation different from that of the Fe-lenses (yellow dotted lines in **Figure 13B**). Moreover, within these morphotypes, no evidence of microbial imprints was recognized. As a result, opaque (*i.e., branched columnar* morphotype) or shiny (*i.e., flat-laminated* and *columnar or pseudo-columnar* morphotypes) bands, depending upon the orientation of the layers (*i.e.,* related to the roughness of the wall surface) and on the presence or absence of detrital minerals, alternate laterally (**Figure 13**). During the growth of the patina the surface becomes progressively flatter (compared to the wall surface), then the last layer that formed shows only two bands, one shiny on the left side and one opaque on the right side of the sample (**Figure 13**). The presence of such bands, parallel to the growth direction of the patinas, and the occurrence of different Mn species (*i.e.,* vernadite: in the opaque bands related to detrital minerals and microbial imprints; and todorokite/ranciéite: in the shiny bands free of detrital minerals and microbial imprints), within the same layers, suggests that the accessory clay minerals and microbial activity may be important factors in controlling MnOx mineralogy, further enhancing the oxidation rate of Mn^{2+} by combining surface catalysis with biological oxidation. In fact, the formation of the poorly crystalline vernadite requires very rapid oxidation of Mn^{2+}, to prevent the formation of more stable MnOx, such as todorokite (Chukhrov, 1980). Other environmental conditions (*e.g.,* pH, Eh, chemistry of the water) cannot explain either the lateral variations of the different morphotypes, or the correlation existing between the morphotypes and the detrital minerals, or even the correlation between the morphotypes and the orientation of the layering. In fact, variations of these environmental parameters would lead to an alternation of layers with different mineralogy/structures (as typically occurs in MnFe nodules and crusts on the ocean floor; see Benites et al., 2018; Marino et al., 2018), and therefore do not appear to be responsible for the recognized distribution of minerals and structures. On the contrary, this spatial distribution points to quite constant environmental conditions, during the growth of the Mn-layers, which change abruptly (toward suboxic conditions) only during the deposition of the Fe-lenses. As well known, the morphology of stromatolite-like deposits strongly depends on sedimentation, grain size of the sediments, nutrient supply, flow velocity, among others (Hickman-Lewis et al., 2019 and references therein). For instance, branching forms develop in less turbulent environments, which facilitate sedimentation; whereas planar forms are produced in more turbulent environments

characterized by lower sedimentation rate (Dupraz et al., 2006 and references therein). Moreover, hydrodynamic conditions set the spatial distribution of shear stress and oxygen availability, promoting specific microbial colonization patterns (Thomen et al., 2017). In this environment, bacteria adhered to the wall surface in low energy zones (*i.e.,* opaque bands), less susceptible to leach, where they found more stable conditions to catalyze Mn^{2+} oxidation (Nealson, 2006). This hypothesis is further supported by the identification of putative predivisional cells, which are usually associated with the attachment of cells to the substrate (Gliesche et al., 2015; Hirsch and Gebers, 2015). Accordingly, the spatial distribution of the different morphotypes points to a strong influence exerted by the geometry of the substrate surface (*i.e.,* morphology of the cave walls) on the hydraulic regime, which, in turn, controls the detrital supply and microbial colonization that trigger the formation of highly disordered vernadite, instead of todorokite and/or ranciéite. This process ultimately affects the spatial distribution of the oxidation state of Mn. Our analyses by Raman mapping (see **Figure 7**) shows that the *flat-laminated* and *columnar or pseudo-columnar* morphotypes (more turbulent local environment) are characterized by the higher average oxidation state of Mn (note that in todorokite/ranciéite Mn occurs under an average oxidation state ~ 3.8, see Chalmin et al., 2009; Post et al., 2003; McKeown and Post, 2001; Post and Bish, 1988). While the *branched columnar* morphotype (associated with a less turbulent local environment, detrital minerals, and bacterially-mediated vernadite), on the other hand, is characterized by the lower average oxidation state of Mn (note that in vernadite Mn occurs under an average oxidation state ~ 3.5, see Manceau et al., 2014).

We suggest that Mn-oxidizing bacteria catalyze the formation of vernadite, a poorly crystalline and disordered compound with high specific surface area and adsorption capacity. Moreover, XRF results show Ni, Zn, Cu, V, and As; consequently, biological activity also controls the partitioning of potentially toxic elements between solid phases and the water system in the studied area.

CONCLUSION

In this work, MnFe patinas from deep inside the *Grotta del Cervo* (Italy) were sampled to study the relationship between mineralogy and oxidation state of Mn, detrital minerals, microbial communities, and morphological features. Our data show that the microbial communities' composition is dominated by Mn^{2+}-oxidizing bacteria and related to Mn-rich environments (*i.e., Bacillus*, *Flavobacterium*, and *Pseudomonas*). Based on our data, we cannot precisely determine which bacteria were directly involved in this process. Nevertheless, this study is a starting point for the identification of bacteria involved in biomineralization processes within this cave. In such an extreme cave environment, bacterial activity catalyzes the oxidation of Mn^{2+} and Fe^{2+} to $Mn^{3+/4+}$ and Fe^{3+}, thereby controlling the partitioning of potentially toxic elements, such as Ni, Zn, Cu, V, and As, between solid phases and the aqueous system. Combining SEM-EDS, XRF, XRPD, FT-IR, and Raman spectroscopy data, we show that these patinas consist of an alternation of Fe-lenses (characterized by a fine-mixture of hematite, goethite, and detrital minerals), and Mn-layers (in which vernadite, todorokite, and/or ranciéite were identified). Moreover, we show an oscillation of Mn and Fe along the growth of the patinas. Based on these results, we hypothesize that the patinas during their growth are recording paleo-floods, alternating oxic and suboxic environments according to the different phases of the flood events, similar to what has been documented in other caves (Rossi et al., 2010; Gázquez et al., 2011). We also recognized a sub-millimetric lamination within the flood events themselves, probably pointing towards normal (seasonal) flood events, higher-than-normal floods (decadal), and a few (secular) extreme events. We thus consider these deposits as indicators of a climate condition characterized by recurrent heavy and prolonged rain periods.

Within the Mn-layers, stromatolite-like structures were identified and related to different mineralogy and oxidation state of Mn, absence/presence of microbial imprints, the abundance of detrital minerals, and layering orientation, namely 1) *branched columnar* morphotype, associated with vernadite and lower oxidation state of Mn, occur in areas rich in detrital minerals, microbial imprints, and voids, 2) *flat-laminated* and 3) *columnar* morphotypes, both associated with todorokite and/or ranciéite and higher oxidation state of Mn, occur in areas with little detrital minerals and free of microbial imprints. These three morphotypes alternate along each Mn-layer as a function of the local layer orientation. All these features suggest that the wall surface's geometry (*i.e.,* roughness) firmly controls the very local hydraulic regime and, in turn, the sedimentation of clay minerals and microbial communities development. Accordingly, in a less turbulent environment, microbial communities development and sedimentation of clays can occur. In this environment, the combination of clay surface catalysis and biological oxidation increases the oxidation rate of Mn^{2+} producing poor-crystalline vernadite, whereas in a more turbulent environment, this catalysis is not possible, and todorokite and/or ranciéite can form.

Our results show that MnFe patinas are precious tools for reconstructing past hydrogeological, mineralogical, and biological processes, particularly for areas where other indicators are lacking, as well as in exoplanetary research. For instance, MnOx have been found on the Mars ground, pointing to a more Earth-like Martian past than previously thought (Lanza et al., 2014, 2016). With this in mind, NASA, ESA/Roscosmos, and CNSA are making great efforts to reconstruct the past Martian environment and seek signs of microbial life, with the Mars 2020, ExoMars 2022, and Tianwen-1 missions, respectively. Therefore, investigating potential microbial-mediated MnOx could be of primary importance to reconstructing the past Martian redox conditions and looking for traces of past or present life.

DATA AVAILABILITY STATEMENT

The nucleotide sequences of the partial 16S rRNA gene segments determined in this study have been deposited in the NCBI database repository, BioProject: PRJNA723830 (https://www.ncbi.nlm.nih.gov/bioproject/PRJNA723830).

AUTHOR CONTRIBUTIONS

SB research coordination, SEM-EDS, XRPD, μXRF, FT-IR, and Raman spectroscopy analyses, data interpretation, writing of the manuscript with support from AC, MDG, CS-J, JDW, and corresponding author; FB scientific supervision, research coordination, manuscript revision, geological data interpretation, SEM-EDS analysis, sampling; AC data interpretation; IV sampling, microbial analysis and interpretation; MP microbial analysis and interpretation; VJ microbial data curation; MDG supervising microbiological work, resources provision; CS-J microbiological data analysis; AS Raman spectroscopy analysis; CM μXRF analysis; LJ μXRF analysis; JDW data interpretation. All the authors have contributed to the scientific discussion of the data and agreed to the submitted version of the manuscript.

ACKNOWLEDGMENTS

This research was conducted in collaboration with the Brazilian Synchrotron Light Laboratory (LNLS), an open national facility belonging to the Brazilian Centre for Research in Energy and Materials (CNPEM) under the supervision of the Brazilian Ministry of Science, Technology, and Innovations (MCTI). Douglas Galante and Carlos Alberto Perez (LNLS - XRF beamline), Priyeshu Srivastava, Mariana Benites, and Ana Martini (IOUSP) are acknowledged for the assistance during XRF measurements. We thank Anas Abbassi (Roma Tre University) for kindly providing the geological map (**Figure 1**), and Roberto Pucci for kindly producing the image shown in **Figure 2**. The Spanish project MINECO CGL 2016-75590-P with ERDF funds is gratefully acknowledged. LJ acknowledge funding from Fundação de Amparo a Pesquisa do Estado de São Paulo (FAPESP) grant 2018/17061-6.

FUNDING

Spanish project MINECO CGL 2016-75590-P with ERDF funds Fundação de Amparo a Pesquisa do Estado de São Paulo (FAPESP) grant 2018/17061-6.

SUPPLEMENTARY MATERIAL

The Supplementary Material for this article can be found online at: https://www.frontiersin.org/articles/10.3389/feart.2021.642667/full#supplementary-material

REFERENCES

Agostini, S., and Piccini, L. (1994). Aspetti geomorfologici ed evolutivi del sistema carsico di Pietrasecca (M. Carseolani - Appennino Centrale, Italia). *Ital. Speleol. Mem.* 5, 61–70

Allward, N. E., Gregory, B. S., Sotddart, A. K., and Gagnon, G. A. (2018). Potential for Manganese Biofouling in Water Transmission Lines Using Model Reactors. *Environ. Sci. Water Res. Technol.* 4, 761–772. doi:10.1039/c8ew00074c

Andrejchuk, V. N., and Klimchouk, A. B. (2001). Geomicrobiology and Redox Geochemistry of the Karstified Miocene gypsum Aquifer, Western Ukraine: The Study from Zoloushka Cave. *Geomicrobiol. J.* 18, 275–295. doi:10.1080/01490450152467796

Arvidson, R. E., Squyres, S. W., Morris, R. V., Knoll, A. H., Gellert, R., Clark, B. C., et al. (2016). High Concentrations of Manganese and Sulfur in Deposits on Murray Ridge, Endeavour Crater, Mars. *Am. Mineral.* 101, 1389–1405. doi:10.2138/am-2016-5599

Balachandran, U., and Eror, N. G. (1982). Raman Spectra of Titanium Dioxide. *J. Solid State. Chem.* 42, 276–282. doi:10.1016/0022-4596(82)90006-8

Barboza, N. R., Amorim, S. S., Santos, P. A., Reis, F. D., Cordeiro, M. M., Guerra-Sá, R., et al. (2015). Indirect Manganese Removal byStenotrophomonassp. andLysinibacillussp. Isolated from Brazilian Mine Water. *Biomed. Res. Int.* 2015, 1–14. doi:10.1155/2015/925972

Bargar, J. R., Tebo, B. M., Bergmann, U., Webb, S. M., Glatzel, P., Chiu, V. Q., et al. (2005). Biotic and Abiotic Products of Mn(II) Oxidation by Spores of the marine Bacillus sp. strain SG-1. *Am. Mineral.* 90, 143–154. doi:10.2138/am.2005.1557

Belli, R., Frisia, S., Borsato, A., Drysdale, R., Hellstrom, J., Zhao, J.-x., et al. (2013). Regional Climate Variability and Ecosystem Responses to the Last Deglaciation in the Northern Hemisphere from Stable Isotope Data and Calcite Fabrics in Two Northern Adriatic Stalagmites. *Quat. Sci. Rev.* 72, 146–158. doi:10.1016/j.quascirev.2013.04.014

Benites, M., Millo, C., Hein, J., Nath, B., Murton, B., Galante, D., et al. (2018). Integrated Geochemical and Morphological Data Provide Insights into the Genesis of Ferromanganese Nodules. *Minerals* 8, 488. doi:10.3390/min8110488

Bernardini, S., Bellatreccia, F., Casanova Municchia, A., Della Ventura, G., and Sodo, A. (2019). Raman Spectra of Natural Manganese Oxides. *J. Raman Spectrosc.* 50, 873–888. doi:10.1002/jrs.5583

Bernardini, S., Bellatreccia, F., Della Ventura, G., Ballirano, P., and Sodo, A. (2020b). Raman Spectroscopy and Laser-Induced Degradation of Groutellite and Ramsdellite, Two Cathode Materials of Technological Interest. *RSC Adv.* 10, 923–929. doi:10.1039/c9ra08662e

Bernardini, S., Bellatreccia, F., Della Ventura, G., and Sodo, A. (2020a). A Reliable Method for Determining the Oxidation State of Manganese at the Microscale in Mn Oxides via Raman Spectroscopy. *Geostand. Geoanal. Res.* 45, 223–244. doi:10.1111/ggr.12361

Berner, R. A. (1981). A New Geochemical Classification of Sedimentary Environments. *J. Sediment. Petrol.* 51, 359–365. doi:10.1306/212F7C7F-2B24-11D7-8648000102C1865D

Bertolani, M., Lugli, S., and Rossi, A. (1994). Petrographic Investigations in the Pietrasecca Cave System (L'Aquila - Central Italy). *Ist. Ital. Speleol. Mem.* 5, 71–83

Bolyen, E., Rideout, J. R., Dillon, M. R., Bokulich, N. A., Abnet, C. C., Al-Ghalith, G. A., et al. (2019). Reproducible, Interactive, Scalable and Extensible Microbiome Data Science Using QIIME 2. *Nat. Biotechnol.* 37, 852–857. doi:10.1038/s41587-019-0209-9

Carmichael, M. J., Carmichael, S. K., Santelli, C. M., Strom, A., and Bräuer, S. L. (2013b). Mn(II)-oxidizing Bacteria Are Abundant and Environmentally Relevant Members of Ferromanganese Deposits in Caves of the Upper Tennessee River Basin. *Geomicrobiol. J.* 30, 779–800. doi:10.1080/01490451.2013.769651

Carmichael, S., Carmichael, M., Strom, A., Johnson, K., Roble, L., Gao, Y., et al. (2013a). Sustained Anthropogenic Impact in Carter Saltpeter Cave, Carter County, Tennessee and the Potential Effects on Manganese Cycling. *J. Cave Karst Stud.* 75, 189–204. doi:10.4311/2012MB0267

Carmichael, S. K., Bräuer, S. L., and Engel, A. S. (2015). "Microbial Diversity and Manganese Cycling: A Review of Manganese-Oxidizing Microbial Cave Communities", *Microbial Life In Cave Systems*," in *Life in Extreme Environments* (Boston: De Gruyter), 137–160.

Chalmin, E., Farges, F., and Brown, G. E. (2009). A Pre-edge Analysis of Mn K-Edge XANES Spectra to Help Determine the Speciation of Manganese in Minerals and Glasses. *Contrib. Mineral. Petrol.* 157, 111–126. doi:10.1007/s00410-008-0323-z

Chaput, D. L., Hansel, C. M., Burgos, W. D., and Santelli, C. M. (2015). Profiling Microbial Communities in Manganese Remediation Systems Treating Coal Mine Drainage. *Appl. Environ. Microbiol.* 81, 2189–2198. doi:10.1128/AEM.03643-14

Chen, S.-C., Chiu, C.-H., Chiu, P.-T., Chen, Y.-C., Lin, Y.-H., Young, C.-C., et al. (2019). Draft Genome Sequence of Manganese-Oxidizing Bacterium

Massilia Sp. Strain Mn16-1_5, Isolated from Serpentine Soil in Taitung, Taiwan. *Microbiol. Resour. Announce* 8, e00694–19. doi:10.1128/MRA.00694-19

Choi, K., Choi, J., Lee, P. A., Roy, N., Khan, R., Lee, H. J., et al. (2020). Alteration of Bacterial Wilt Resistance in Tomato Plant by Microbiota Transplant. *Front. Plant Sci.* 11, 1186. doi:10.3389/fpls.2020.01186

Chukhrov, F. V., Gorshkov, A. I., Rudnitskaya, Y. S., Berezovskaya, V. V., and Sivtsov, A. V. (1978). On Vernadite. *Bull. Acad. Sci. USSR Ser. Geol.* 6, 5–19.

Chukhrov, F. V. (1980). On Vernadite. *Int. Geol. Rev.* 22, 58–74. doi:10.1080/00206818209466863

Columbu, A., Chiarini, V., Spötl, C., Benazzi, S., Hellstrom, J., Cheng, H., et al. (2020). Speleothem Record Attests to Stable Environmental Conditions during Neanderthal-Modern Human Turnover in Southern Italy. *Nat. Ecol. Evol.* 4, 1188–1195. doi:10.1038/s41559-020-1243-1

Columbu, A., De Waele, J., Forti, P., Montagna, P., Picotti, V., Pons-Branchu, E., et al. (2015). Gypsum Caves as Indicators of Climate-Driven River Incision and Aggradation in a Rapidly Uplifting Region. *Geology* 43, 539–542. doi:10.1130/G36595.1

Columbu, A., Drysdale, R., Capron, E., Woodhead, J., De Waele, J., Sanna, L., et al. (2017). Early Last Glacial Intra-interstadial Climate Variability Recorded in a Sardinian Speleothem. *Quat. Sci. Rev.* 169, 391–397. doi:10.1016/j.quascirev.2017.05.007

Columbu, A., Sauro, F., Lundberg, J., Drysdale, R., and De Waele, J. (2018). Palaeoenvironmental Changes Recorded by Speleothems of the Southern Alps (Piani Eterni, Belluno, Italy) during Four Interglacial to Glacial Climate Transitions. *Quat. Sci. Rev.* 197, 319–335. doi:10.1016/j.quascirev.2018.08.006

Columbu, A., Spötl, C., De Waele, J., Yu, T.-L., Shen, C.-C., and Gázquez, F. (2019). A Long Record of MIS 7 and MIS 5 Climate and Environment from a Western Mediterranean Speleothem (SW Sardinia, Italy). *Quat. Sci. Rev.* 220, 230–243. doi:10.1016/j.quascirev.2019.07.023

Cornaggia, F., Bernardini, S., Giorgioni, M., Silva, G. L. X., Nagy, A. I. M., and Jovane, L. (2020). Abyssal Oceanic Circulation and Acidification during the Middle Eocene Climatic Optimum (MECO). *Sci. Rep.* 10, 1–9. doi:10.1038/s41598-020-63525-3

Cosentino, D., Carboni, M. G., Cipollari, P., Di Bella, L., Florindo, F., Laurenzi, M. A., et al. (1997). Integrated Stratigraphy of the Tortonian/Messinian Boundary: The Pietrasecca Composite Section (Centra Appenines, Italy). *Eclogae Geol. Helv.* 90, 229–224.

Cunningham, K. I., Northup, D. E., Pollastro, R. M., Wright, W. G., and LaRock, E. J. (1995). Bacteria, Fungi and Biokarst in Lechuguilla Cave, Carlsbad Caverns National Park, New Mexico. *Environ. Geol.* 25, 2–8. doi:10.1007/BF01061824

de Faria, D. L. A., and Lopes, F. N. (2007). Heated Goethite and Natural Hematite: Can Raman Spectroscopy Be Used to Differentiate Them? *Vib. Spectrosc.* 45, 117–121. doi:10.1016/j.vibspec.2007.07.003

Drysdale, R. N., Hellstrom, J. C., Zanchetta, G., Fallick, A. E., Sanchez Goni, M. F., Couchoud, I., et al. (2009). Evidence for Obliquity Forcing of Glacial Termination II. *Science* 325, 1527–1531. doi:10.1126/science.1170371

Dupraz, C., Pattisina, R., and Verrecchia, E. P. (2006). Translation of Energy into Morphology: Simulation of Stromatolite Morphospace Using a Stochastic Model. *Sediment. Geol.* 185, 185–203. doi:10.1016/j.sedgeo.2005.12.012

Ertl, A., Pertlik, F., Prem, M., Post, J. E., Kim, S. J., Brandstä tter, F., et al. (2005). Rancieite Crystals from Friesach, Carinthia, Austria. *Eur. J. Mineral.* 17, 163–172. doi:10.1127/0935-1221/2005/0017-0163

Fairchild, I. J., Smith, C. L., Baker, A., Fuller, L., Spötl, C., Mattey, D., et al. (2006). Modification and Preservation of Environmental Signals in Speleothems. *Earth-Sci. Rev.* 75, 105–153. doi:10.1016/j.earscirev.2005.08.003

Farrugia, C., Borg, R. P., Ferrara, L., and Buhagiar, J. (2019). The Application of *Lysinibacillus Sphaericus* for Surface Treatment and Crack Healing in Mortar. *Front. Built Environ.* 5, 62. doi:10.3389/fbuil.2019.00062

Feng, X. H., Zhu, M., Ginder-Vogel, M., Ni, C., Parikh, S. J., and Sparks, D. L. (2010). Formation of Nano-Crystalline Todorokite from Biogenic Mn Oxides. *Geochim. Cosmochim. Acta* 74, 3232–3245. doi:10.1016/j.gca.2010.03.005

Fonollá, C., Sanz, E., and Menéndez-Pidal, I. (2020). Lateral Ferruginous Groundwater Transfer as the Origin of the Iron Crusts in Caves: a Case Study. *J. Cave Karst Stud.* 82, 183–197. doi:10.4311/2019ES0143

Forti, P. (1994). I fenomeni concrezionari nelle grotte del Cervo e dell'Ovito a Pietrasecca. *Ist. Ital. Speleol. Mem.* 5, 85–96.

Francis, C. A., and Tebo, B. M. (2002). Enzymatic Manganese(II) Oxidation by Metabolically Dormant Spores of Diverse Bacillus Species. *Appl. Environ. Microbiol.* 68, 874–880. doi:10.1128/AEM.68.2.874–880.200210.1128/aem.68.2.874-880.2002

Frierdich, A. J., Hasenmueller, E. A., and Catalano, J. G. (2011). Composition and Structure of Nanocrystalline Fe and Mn Oxide Cave Deposits: Implications for Trace Element Mobility in Karst Systems. *Chem. Geol.* 284, 82–96. doi:10.1016/j.chemgeo.2011.02.009

Frisia, S., Borsato, A., Mangini, A., Spötl, C., Madonia, G., and Sauro, U. (2006). Holocene Climate Variability in Sicily from a Discontinuous Stalagmite Record and the Mesolithic to Neolithic Transition. *Quat. Res.* 66, 388–400. doi:10.1016/j.yqres.2006.05.003

Frisia, S., Borsato, A., Spötl, C., Villa, I. M., and Cucchi, F. (2005). Climate Variability in the SE Alps of Italy over the Past 17 000 Years Reconstructed from a Stalagmite Record. *Boreas* 34, 445–455. doi:10.1080/03009480500231336

Gázquez, F., Calaforra, J. M., and Forti, P. (2011). Black Mn-Fe Crusts as Markers of Abrupt Palaeoenvironmental Changes in El Soplao Cave (Cantabria, Spain). *Int. J. Speleol.* 40, 163–169. doi:10.5038/1827-806X.40.2.8

Ghosh, S., Mohanty, S., Nayak, S., Sukla, L. B., and Das, A. P. (2016). Molecular Identification of Indigenous Manganese Solubilising Bacterial Biodiversity from Manganese Mining Deposits. *J. Basic Microbiol.* 56, 254–262. doi:10.1002/jobm.201500477

Gliesche, C., Fesefeldt, A., and Hirsch, P. (2015). Hyphomicrobium. *Bergey's Manual of Systematics of Archaea and Bacteria*. New York: Springer-Verlag, 1–34. doi:10.1002/9781118960608.gbm00820

Gonzalez-Pimentel, J. L., Martin-Pozas, T., Jurado, V., Miller, A. Z., Caldeira, A. T., Fernandez-Lorenzo, O., et al. (2021). Prokaryotic Communities from a Lava Tube Cave in La Palma Island (Spain) Are Involved in the Biogeochemical Cycle of Major Elements. *PeerJ* 9, e11386. doi:10.7717/peerj.11386

Gradziński, M., Banaś, M., and Uchman, A. (1995). Biogenic Origin of Manganese Flowstones from Jaskinia Czarna Cave, Tatra mts., Western Carpathians. *Ann. Soc. Geol. Pol.* 65, 19–27.

Hammer, Ø., Harper, D. A. T., and Ryan, P. D. (2001). Past: Paleontological Statistics Software Package for Education and Data Analysis. *Palaeontol. Electronica* 4, 1–9.

He, J., Zhang, L., Jin, S., Zhu, Y., and Liu, F. (2008). Bacterial Communities inside and Surrounding Soil Iron-Manganese Nodules. *Geomicrobiol. J.* 25, 14–24. doi:10.1080/01490450701829014

Hein, J. R., Konstantinova, N., Mikesell, M., Mizell, K., Fitzsimmons, J. N., Lam, P. J., et al. (2017). Arctic Deep Water Ferromanganese-Oxide Deposits Reflect the Unique Characteristics of the Arctic Ocean. *Geochem. Geophys. Geosyst.* 18, 3771–3800. doi:10.1002/2017GC007186

Hem, J. D. (1972). Chemical Factors that Influence the Availability of Iron and Manganese in Aqueous Systems. *Geol. Soc. Am. Bull.* 83, 443–450. doi:10.1130/0016-7606(1972)83[443:CFTITA]2.0.CO;2

Hem, J. D. (1963). Chemical Equilibria Affecting the Behavior of Manganese in Natural Water. *Int. Assoc. Sci. Hydrol. Bull.* 8, 30–37. doi:10.1080/02626666309493334

Hickman-Lewis, K., Gautret, P., Arbaret, L., Sorieul, S., De Wit, R., Foucher, F., et al. (2019). Mechanistic Morphogenesis of Organo-Sedimentary Structures Growing under Geochemically Stressed Conditions: Keystone to Proving the Biogenicity of Some Archaean Stromatolites? *Geosciences* 9, 359. doi:10.3390/geosciences9080359

Hill, C., and Forti, P. (1997). *Cave Minerals of the World*. Huntsville: National Speleological Society.

Hirsch, P., and Gebers, R. (2015). Pedomicrobium Aristovskaya 1961, 957 AL Emend. Gebers and Beese 1988, 305. *Bergey's Manual of Systematics of Archaea and Bacteria*. New York: Springer-Verlag, 527–538.

Hou, D., Zhang, P., Wei, D., Zhang, J., Yan, B., Cao, L., et al. (2020). Simultaneous Removal of Iron and Manganese from Acid Mine Drainage by Acclimated Bacteria. *J. Hazard. Mater.* 396, 122631. doi:10.1016/j.jhazmat.2020.122631

Itcus, C., Pascu, M. D., Lavin, P., Perşoiu, A., Iancu, L., and Purcarea, C. (2018). Bacterial and Archaeal Community Structures in Perennial Cave Ice. *Sci. Rep.* 8, 15671. doi:10.1038/s41598-018-34106-2

Jiang, S., Kim, D.-G., Kim, J.-H., and Ko, S.-O. (2010). Characterization of the Biogenic Manganese Oxides Produced by *Pseudomonas Putida* Strain MnB1. *Environ. Eng. Res.* 15, 183–190. doi:10.4491/eer.2010.15.4.183

Jurado, V., Gonzalez-Pimentel, J. L., Miller, A. Z., Hermosin, B., D'Angeli, I. M., Tognini, P., et al. (2020). Microbial Communities in Vermiculation Deposits from an Alpine Cave. *Front. Earth Sci.* 8, 586248. doi:10.3389/feart.2020.586248

Kim, H.-S., Pastén, P. A., Gaillard, J.-F., and Stair, P. C. (2003). Nanocrystalline Todorokite-like Manganese Oxide Produced by Bacterial Catalysis. *J. Am. Chem. Soc.* 125, 14284–14285. doi:10.1021/ja0375784

Koschinsky, A., and Halbach, P. (1995). Sequential Leaching of marine Ferromanganese Precipitates: Genetic Implications. *Geochim. Cosmochim. Acta* 59, 5113–5132. doi:10.1016/0016-7037(95)00358-4

Kotula, P., Andreychouk, V., Andreychouk, V., Pawlyta, J., Marynowski, L., and Jendrzejewska, I. (2019). Genesis of Iron and Manganese Sediments in Zoloushka Cave (Ukraine/Moldova) as Revealed by $\delta^{13}C$ Organic Carbon. *Int. J. Speleol.* 48, 221–235. doi:10.5038/1827-806X.48.3.2255

Lanza, N. L., Fischer, W. W., Wiens, R. C., Grotzinger, J., Ollila, A. M., Cousin, A., et al. (2014). High Manganese Concentrations in Rocks at Gale Crater, Mars. *Geophys. Res. Lett.* 41, 5755–5763. doi:10.1002/2014GL060329

Lanza, N. L., Wiens, R. C., Arvidson, R. E., Clark, B. C., Fischer, W. W., Gellert, R., et al. (2016). Oxidation of Manganese in an Ancient Aquifer, Kimberley Formation, Gale Crater, Mars. *Geophys. Res. Lett.* 43, 7398–7407. doi:10.1002/2016GL069109

Lee, S., Xu, H., Xu, W., and Sun, X. (2019). The Structure and crystal Chemistry of Vernadite in Ferromanganese Crusts. *Acta Crystallogr., Sect B: Struct. Sci., Cryst. Eng. Mater.* 4, 591–598. doi:10.1107/S2052520619006528

Lee, Y. S., Kim, H. J., and Park, W. (2017). Non-ureolytic Calcium Carbonate Precipitation by *Lysinibacillus* Sp. YS11 Isolated from the Rhizosphere of *Miscanthus Sacchariflorus*. *J. Microbiol.* 55, 440–447. doi:10.1007/s12275-017-7086-z

Liu, H., Song, Y., Chen, F., Zheng, S., and Wang, G. (2013). *Lysinibacillus Manganicus* Sp. nov., Isolated from Manganese Mining Soil. *Int. J. Syst. Evol. Microbiol.* 63, 3568–3573. doi:10.1099/ijs.0.050492-0

Lozano, R. P., and Rossi, C. (2012). Exceptional Preservation of Mn-Oxidizing Microbes in Cave Stromatolites (El Soplao, Spain). *Sediment. Geol.* 255–256, 42–55. doi:10.1016/j.sedgeo.2012.02.003

Manceau, A., Lanson, M., and Takahashi, Y. (2014). Mineralogy and crystal Chemistry of Mn, Fe, Co, Ni, and Cu in a Deep-Sea Pacific Polymetallic Nodule. *Am. Mineral.* 99, 2068–2083. doi:10.2138/am-2014-4742

Marino, E., González, F., Lunar, R., Reyes, J., Medialdea, T., Castillo-Carrión, M., et al. (2018). High-Resolution Analysis of Critical Minerals and Elements in Fe-Mn Crusts from the Canary Island Seamount Province (Atlantic Ocean). *Minerals* 8, 285. doi:10.3390/min8070285

McKenzie, R. (1980). The Adsorption of lead and Other Heavy Metals on Oxides of Manganese and Iron. *Soil Res.* 18, 61–73. doi:10.1071/sr9800061

McKeown, D. A., and Post, J. E. (2001). Characterization of Manganese Oxide Mineralogy in Rock Varnish and Dendrites Using X-ray Absorption Spectroscopy. *Am. Mineral.* 86, 701–713. doi:10.2138/am-2001-5-611

Meier, A., Kastner, A., Harries, D., Wierzbicka-Wieczorek, M., Majzlan, J., Büchel, G., et al. (2017). Calcium Carbonates: Induced Biomineralization with Controlled Macromorphology. *Biogeosciences* 14, 4867–4878. doi:10.5194/bg-14-4867-2017

Mitchell, A. C., Espinosa-Ortiz, E. J., Parks, S. L., Phillips, A. J., Cunningham, A. B., and Gerlach, R. (2019). Kinetics of Calcite Precipitation by Ureolytic Bacteria under Aerobic and Anaerobic Conditions. *Biogeosciences* 16, 2147–2161. doi:10.5194/bg-16-2147-2019

Naeher, S., Gilli, A., North, R. P., Hamann, Y., and Schubert, C. J. (2013). Tracing Bottom Water Oxygenation with Sedimentary Mn/Fe Ratios in Lake Zurich, Switzerland. *Chem. Geol.* 352, 125–133. doi:10.1016/j.chemgeo.2013.06.006

Nealson, K. H. (2006). The Manganese-Oxidizing Bacteria. *The Prokaryotes*. New York: Springer, 222–231. doi:10.1007/0-387-30745-1_11

Northup, D. E., Barns, S. M., Yu, L. E., Spilde, M. N., Schelble, R. T., Dano, K. E., et al. (2003). Diverse Microbial Communities Inhabiting Ferromanganese Deposits in Lechuguilla and Spider Caves. *Environ. Microbiol.* 5, 1071–1086. doi:10.1046/j.1462-2920.2003.00500.x

Northup, D. E., Dahm, C. N., Melim, L. A., Spilde, M. N., Crossey, L. J., Lavoie, K. H., et al. (2000). Evidence for Geomicrobiological Interactions in Guadalupe Caves. *J. Cave Karst Stud.* 62, 80–90.

Ortega-Villamagua, E., Gudiño-Gomezjurado, M., and Palma-Cando, A. (2020). Microbiologically Induced Carbonate Precipitation in the Restoration and Conservation of Cultural Heritage Materials. *Molecules* 25, 5499. doi:10.3390/molecules25235499

Oscarson, D. W., Huang, P. M., Liaw, W. K., and Hammer, U. T. (1983). Kinetics of Oxidation of Arsenite by Various Manganese Dioxides. *Soil Sci. Soc. Am. J.* 47, 644–648. doi:10.2136/sssaj1983.03615995004700040007x

Papier, S., Baele, J. M., Gillan, D., Barriquand, J., and Barriquand, L. (2011). Manganese Geomicrobiology of the Black Deposits from the Azé Cave, Saône-Et-Loire, France. *Quaternaire* 4, 297–305.

Pasić, L., Kovce, B., Sket, B., and Herzog-Velikonja, B. (2010). Diversity of Microbial Communities Colonizing the walls of a Karstic Cave in Slovenia. *FEMS Microbiol. Ecol.* 71, 50–60. doi:10.1111/j.1574-6941.2009.00789.x

Post, J. E., and Bish, D. L. (1988). Rietveld Refinement of the Todorokite Structure. *Am. Mineral.* 73, 861–869.

Post, J. E., Heaney, P. J., and Hanson, J. (2003). Synchrotron X-ray Diffraction Study of the Structure and Dehydration Behavior of Todorokite. *Am. Mineral.* 88, 142–150. doi:10.2138/am.2007.213410.2138/am-2003-0117

Post, J. E. (1999). Manganese Oxide Minerals: Crystal Structures and Economic and Environmental Significance. *Proc. Natl. Acad. Sci.* 96, 3447–3454. doi:10.1073/pnas.96.7.3447

Postpischl, D., Agostini, S., Forti, P., and Quinif, Y. (1991). Palaeoseismicity from karst sediments: the "Grotta del Cervo" cave case study (Central Italy). *Tectonophysics* 193, 33–44. doi:10.1016/0040-1951(91)90186-v

Potter, R. M., and Rossman, G. R. (1979). The Tetravalent Manganese Oxides: Identification, Hydration, and Structural Relationships by Infrared Spectroscopy. *Am. Mineral.* 64, 1199–1218.

Reeksting, B. J., Hoffmann, T. D., Tan, L., Paine, K., and Gebhard, S. (2020). In-depth Profiling of Calcite Precipitation by Environmental Bacteria Reveals Fundamental Mechanistic Differences with Relevance to Application. *Appl. Environ. Microbiol.* 86, e02739-19. doi:10.1128/AEM.02739-19

Regattieri, E., Zanchetta, G., Isola, I., Zanella, E., Drysdale, R. N., Hellstrom, J. C., et al. (2019). Holocene Critical Zone Dynamics in an Alpine Catchment Inferred from a Speleothem Multiproxy Record: Disentangling Climate and Human Influences. *Sci. Rep.* 9, 1. doi:10.1038/s41598-019-53583-7

Robertson, A. H. F., Necdet, M., Raffi, I., and Chen, G. (2019). Early Messinian Manganese Deposition in NE Cyprus Related to Cyclical Redox Changes in a Silled Hemipelagic basin Prior to the Mediterranean Salinity Crisis. *Sediment. Geol.* 385, 126–148. doi:10.1016/j.sedgeo.2019.03.009

Rossi, C., Lozano, R. P., Isanta, N., and Hellstrom, J. (2010). Manganese Stromatolites in Caves: El Soplao (Cantabria, Spain). *Geology* 38, 1119–1122. doi:10.1130/G31283.1

Roy, S., Nicholson, K., Hein, J. R., Buhn, B., and Dasgupta, S. (1997). Genetic Diversity of Manganese Deposition in the Terrestrial Geological Record, *Geol. Soc. Lond. Spec. Publications*. *Manganese Mineralization: Geochemistry and Mineralogy of Terrestrial and Marine Deposits*, 119. London: Geological Society Special Publication, 5–27. doi:10.1144/gsl.sp.1997.119.01.02

Saiz-Jimenez, C., Miller, A. Z., Martin-Sanchez, P. M., and Hernandez-Marine, M. (2012). Uncovering the Origin of the Black Stains in Lascaux Cave in France. *Environ. Microbiol.* 14, 3220–3231. doi:10.1111/1462-2920.12008

Sjöberg, S., Callac, N., Allard, B., Smittenberg, R. H., and Dupraz, C. (2018). Microbial Communities Inhabiting a Rare Earth Element Enriched Birnessite-type Manganese deposit in the Ytterby Mine, Sweden. *Geomicrobiol. J.* 35, 657–674. doi:10.1080/01490451.2018.1444690

Spilde, M. N., Northup, D. E., Boston, P. J., Schelble, R. T., Dano, K. E., Crossey, L. J., et al. (2005). Geomicrobiology of Cave Ferromanganese Deposits: a Field and Laboratory Investigation. *Geomicrobiol. J.* 22, 99–116. doi:10.1080/01490450590945889

Spiro, T. G., Bargar, J. R., Sposito, G., and Tebo, B. M. (2010). Bacteriogenic Manganese Oxides. *Acc. Chem. Res.* 43, 2–9. doi:10.1021/ar800232a

Stoppa, F., Woolley, A. R., and Cundari, A. (2002). Extension of the melilite-carbonatite province in the Apennines of Italy: the kamafugite of Grotta del Cervo, Abruzzo. *Mineral. Mag.* 66, 555–574. doi:10.1180/0026461026640049

Tebo, B. M., Bargar, J. R., Clement, B. G., Dick, G. J., Murray, K. J., Parker, D., et al. (2004). BIOGENIC MANGANESE OXIDES: Properties and Mechanisms of Formation. *Annu. Rev. Earth Planet. Sci.* 32, 287–328. doi:10.1146/annurev.earth.32.101802.120213

Tebo, B. M., Johnson, H. A., McCarthy, J. K., and Templeton, A. S. (2005). Geomicrobiology of Manganese(II) Oxidation. *Trends Microbiol.* 13, 421–428. doi:10.1016/j.tim.2005.07.009

Thomen, P., Robert, J., Monmeyran, A., Bitbol, A.-F., Douarche, C., and Henry, N. (2017). Bacterial Biofilm under Flow: First a Physical Struggle to Stay, Then a Matter of Breathing. *PLoS One* 12, e0175197. doi:10.1371/journal.pone.0175197

Vaccarelli, I., Matteucci, F., Pellegrini, M., Bellatreccia, F., and Del Gallo, M. (2021). Exploring Microbial Biosignatures in Mn-Deposits of Deep Biosphere: A Preliminary Cross-Disciplinary Approach to Investigate Geomicrobiological Interactions in a Cave in Central Italy. *Front. Earth Sci.* 9, 590257. doi:10.3389/feart.2021.590257

Vanghi, V., Borsato, A., Frisia, S., Drysdale, R., Hellstrom, J., and Bajo, P. (2018). Climate Variability on the Adriatic Seaboard during the Last Glacial Inception and MIS 5c from Frasassi Cave Stalagmite Record. *Quat. Sci. Rev.* 201, 349–361. doi:10.1016/j.quascirev.2018.10.023

Villalobos, M., Toner, B., Bargar, J., and Sposito, G. (2003). Characterization of the Manganese Oxide Produced by *Pseudomonas Putida* Strain MnB1. *Geochim. Cosmochim. Acta* 67, 2649–2662. doi:10.1016/S0016-7037(03)00217-5

White, W. B., Vito, C., and Scheetz, B. E. (2009). The Mineralogy and Trace Element Chemistry of Black Manganese Oxide Deposits from Caves. *J. Cave Karst Stud.* 71, 136–143.

Wiseschart, A., Mhuantong, W., Tangphatsornruang, S., Chantasingh, D., and Pootanakit, K. (2019). Shotgun Metagenomic Sequencing from Manao-Pee Cave, Thailand, Reveals Insight into the Microbial Community Structure and its Metabolic Potential. *BMC Microbiol.* 19, 144. doi:10.1186/s12866-019-1521-8

Xu, Z. G., Ding, Y., Huang, H. M., Wu, L., Zhao, Y. L., and Yang, G. Y. (2019). Biosorption Characteristics of Mn (II) by Bacillus Cereus Strain HM-5 Isolated from Soil Contaminated by Manganese Ore. *Pol. J. Environ. Stud.* 28, 1–10. doi:10.15244/pjoes/84838

Zanchetta, G., Drysdale, R. N., Hellstrom, J. C., Fallick, A. E., Isola, I., Gagan, M. K., et al. (2007). Enhanced Rainfall in the Western Mediterranean during Deposition of Sapropel S1: Stalagmite Evidence from Corchia Cave (Central Italy). *Quat. Sci. Rev.* 26, 279–286. doi:10.1016/j.quascirev.2006.12.003

Conflict of Interest: The authors declare that the research was conducted in the absence of any commercial or financial relationships that could be construed as a potential conflict of interest.

Publisher's Note: All claims expressed in this article are solely those of the authors and do not necessarily represent those of their affiliated organizations, or those of the publisher, the editors and the reviewers. Any product that may be evaluated in this article, or claim that may be made by its manufacturer, is not guaranteed or endorsed by the publisher.